MATERIAL DESIGN AND DURABILITY CHARACTERIZATION OF "NON-BRITTLE" GEOPOLYMER

A Thesis

Presented to

The Faculty of the Department of Civil and Environmental Engineering

University of Houston

In Partial Fulfillment

Of the Requirements for the degree

Master of Science

In Civil Engineering

by

Yun-Chen Wu

December 2015

MATERIAL DESIGN AND DURABILITY CHARACTERIZATION OF "NON-BRITTLE" GEOPOLYMER

Yun-Chen Wu

Approved:

Chair of the Committee
Dr. Mo Li, Assistant Professor,
Civil and Environmental Engineering

Committee Members:

Dr. Yandi Hu, Assistant Professor,
Civil and Environmental Engineering

Dr. Ashutosh Agrawal, Assistant Professor,
Mechanical Engineering

Dr. Suresh K. Khator, Associate Dean,
Cullen College of Engineering

Dr. Roberto Ballarini, Department Chair,
Civil and Environmental Engineering

Acknowledgements

I would like to express my gratitude to my academic advisor Professor Mo Li for her guidance through the process and her patience for providing advices when I had difficulties on my work. She also offered me sufficient resources to do my research study that let my research work efficiently. In addition, I appreciate Dr. Yandi Hu and Dr. Ashutosh Agrawal for serving on my thesis committee.

I gratefully acknowledge my fellow graduate students Prakash Bhat, Xiaopeng Li, Shuai Fan and Ing Lim for helping me with the experimental and analytical work.

In the end, I would like to thank my family and friends for their encouragement and assistances.

MATERIAL DESIGN AND DURABILITY CHARACTERIZATION OF "NON-BRITTLE" GEOPOLYMER

An Abstract

of a

Thesis

Presented to

The Faculty of the Department of Civil and Environmental Engineering

University of Houston

In Partial Fulfillment

Of the Requirements for the degree

Master of Science

In Civil Engineering

by

Yun-Chen Wu

December 2015

Abstract

Geopolymers are inorganic polymers that have resulted in wide scientific interest and broad development of applications. They possess intriguing characteristics that bridge polymer science and ceramics. Many inexpensive earth-abundant minerals and industrial wastes can form geopolymers; this diversity enables a large palette of suitable ingredients to be selected to achieve specific properties, offering a variety of possibilities for material design. The microstructure of fully reacted K-poly(sialate-siloxo) type geopolymer is nanoporous and sponge-like, consisting of nanoparticulates ranging from 5-15 nm separated by nanopores on the order of 3 to 10 nm. The nanoparticulates features dimensions suggesting a macromolecule of definite size. Such characteristic microstructure of geopolymers leads to their unique chemical and mechanical features. While geopolymers provide great potential for applications in many fields, their long-term performance remains unaddressed. Also, the inherent brittleness of geopolymers limits their durability; inevitable cracking can be the result of one or a combination of mechanical and environmental factors. In this thesis, we aim at designing a new category of geopolymers with a “non-brittle” behavior, and understanding the mechanical and chemical responses of geopolymer to various environmental conditions including shrinkage, elevated temperature, water permeation, and corrosion of embedded steel.

Table of Contents

List of Figures

List of Tables

CHAPTER 1: INTRODUCTION

1.1 Background

Since human was aware that emission of carbon dioxide (CO_2) causes a great part of global warming and environmental pollution, people started looking for several ways in order to cut down the amount of emission of CO_2.

In the field of Civil Engineering, people usually use cement as the base material for concrete. However, in the process of producing cement, each ton of cement accompanied by emission of CO_2 varies between 0.05 and 0.13 tons. The cement consumption in United States was around 1,054,870 tons in the past 10 years (Figure 1.1) that caused approximately 7% of total greenhouse gas emission. Apparently, by lowering the rate of material consumption can reduce the impact for the greenhouse gas emission.

Fly ash (FA), one of the residues generated by coal combustion. It was used partially replace the amount of cement in concrete. People no longer need to produce as much cement as past since FA is a waste material that using it can prevent material consumption during manufacture. Take geopolymer concrete for example, people can not only use FA for building the matrix of concrete, but also avoid using any cement in the process of casting concrete.

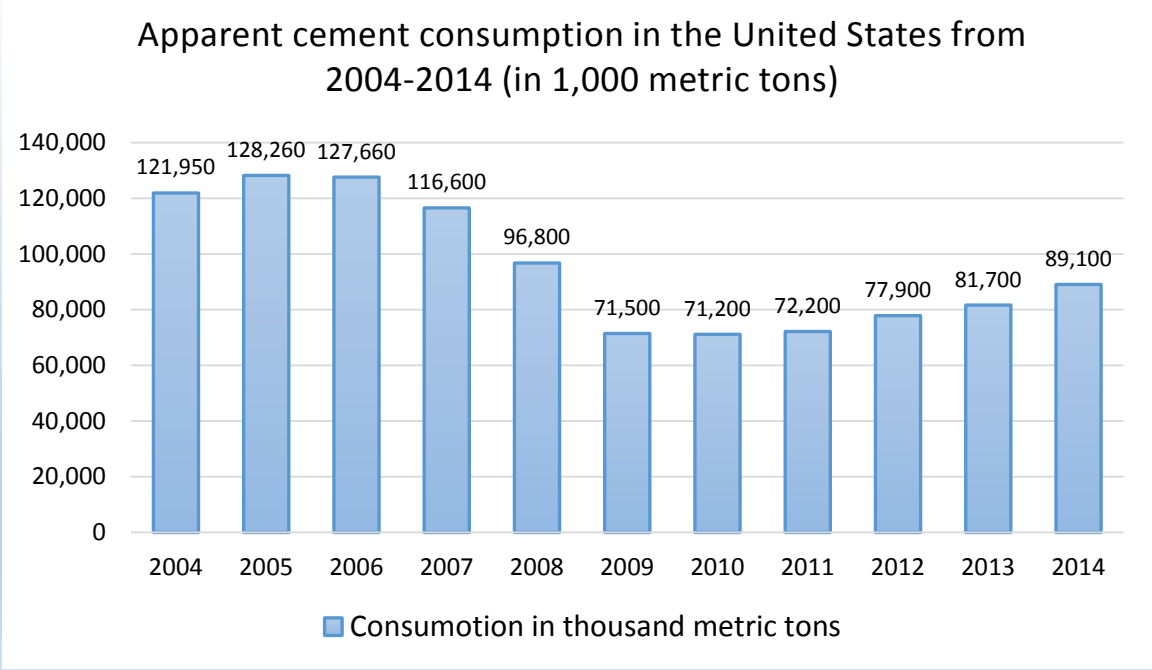

Figure 1.1: Apparent cement consumption in the United States from 2004 to 2014 (US Geological Survey, Statistica 2015)

1.2 Motivation

Since Ordinary Portland Cement (OPC) based concrete has very brittle behavior. In order to increase the ductility in such a brittle material, people created a new type of material which designed based on micromechanics and fracture mechanics theory to reach higher tensile ductility called engineered cementitious composite (ECC). It is a mortar-based composite with selected short random polymer fibers.

Conventional OPC-based concrete is lack of durability and failure under strain due to its brittle behavior. This is one of the reasons that scientists put efforts on developing ECC as the result it can deform under strain. For example, the tensile strain capacity of ECC, a micromechanics-based designed ultra-ductile strain-hardening cementitious composite (SHCC) is about 300% higher than OPC. In the last decades, the development SHCC of has caught people's attention.

While geopolymer concrete has good strength and excellent environmentally-friendly material behavior, the inherent property is as brittle as OPC should be noticed. Motohiro Ohno and Victor C. Li developed strain-hardening ductile fiber geopolymer composites (FGC) by using randomly oriented short Poly-Vinyl Alcohol (PVA) fibers. Due to tight crack and fiber, they achieved very high tensile ductility performances over 4% [5].

The mechanical properties have already been explored in some studies. However, there is still lack of attempts to assess other durability properties of FGC. In this study, the other characteristic of FGC includes temperature resistance, alkali-silica reaction, shrinkage, water permeability and corrosion will be discussed.

1.3 Literature Review

Geopolymer, the term is described an alternative cementitious material which has ceramic-like properties was first introduced to the world by Joseph Davidovits in 1978 [2,3] and lots of scientific researchers and industry disciplines started putting their heart to explore the properties and usage. T.F. Yen [1] classified geopolymer into two groups, pure inorganic geopolymers and organic containing geopolymers. Generally speaking, a chemical compound which is consisted of repeating units such as silico-oxide (-Si-O-Si-O-), silico-aluminate (-Si-O-Al-O-), etc. can be regarded as a geopolymer.

In cement-based concrete matrix, the mainly reaction is hydration which means cement only needs water to react and create strength. For geopolymer, the mixture of alkali solution and alkali silicate solution which is used as an activator to trigger the reaction between fly-ash and blast furnace slag. Unlike cement-based matrix needs roughly 28 days for hydration, geopolymerization process gives a conversely rapid

reaction with high strength solidification. Besides, depending on the starting materials and reaction condition that C-S-H and C-A-H phases might also be originated. Davidovits, provided an empirical formula for geopolymer as (equation (1.1)) [4]

$$Mn\ \{-(SiO_2)_z\text{-}AlO_2\}_n \bullet wH_2O, \tag{1.1}$$

where M means cation like K^+, Na^+ or Ca^{2+}, n is the degree of polycondensation and z could be 1, 2 or 3. The definition proposed by Davidovits was "the geopolymer material is a material originated by inorganic polycondensation." The network is configured of SiO_4 and AlO_4 tetrahedrons and be gathered by oxygen (Figure 1.2 & Figure 1.3) [2, 3, 4]. It forms chains or rings united by Si-O-Al, etc. Positive ions must compensate the negative charges. Davidovits claimed that not all of the alkaline activated material equal to geopolymer. Geopolymer is a subset of alkaline activated material and it must have to be in line with the previous definition.

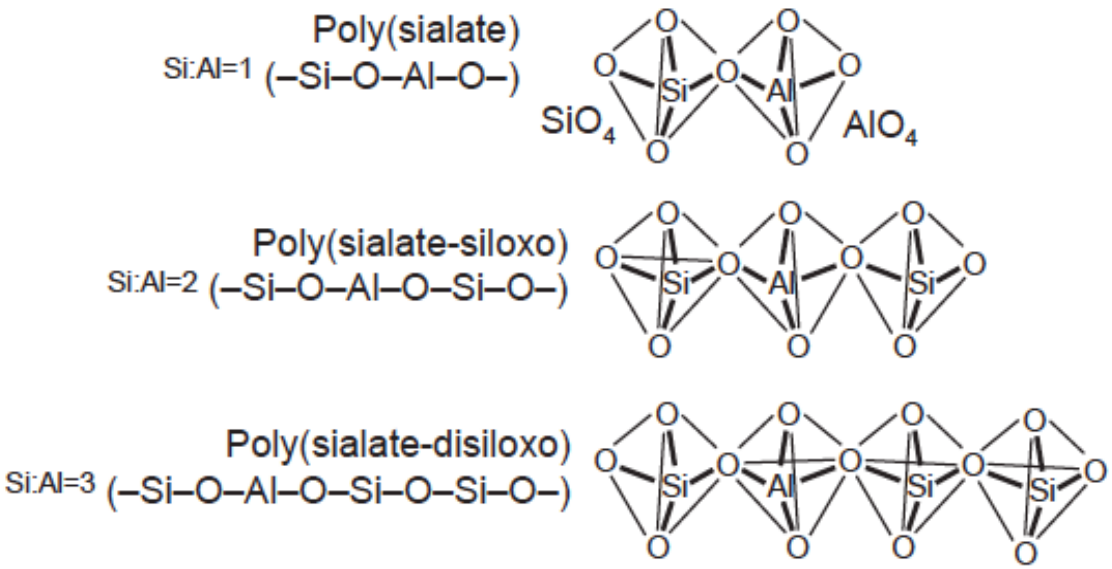

Figure 1.2: Davidovits terminology [2]

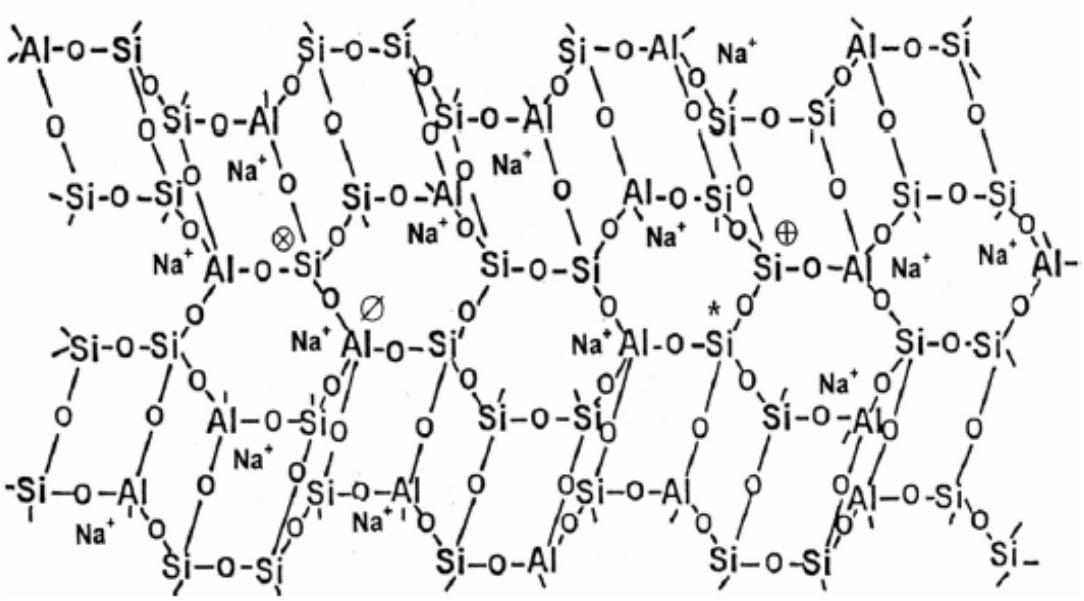

Figure 1.3: Geopolymer structure [2]

Silicon (Si) and aluminum (Al) could be used as a source material which rich present in FA that can react with alkaline liquid such as the admixture of sodium hydroxide (NaOH) solution and sodium silicate (Na_2SiO_3) solution. This alkaline activation is a chemical process called geopolymerization that gives a rapid structure change in those specific materials to form concrete frameworks. Geopolymerization process include three stages:(I) destruction, (II) polymerization, (III) stabilization. In the first stage OH^- anions begin attacking on Si-O and Al-O bonds that exist on FA particle surface and break it down. The second stage, the destruction products in the system will polymerize into gels. In the last stage, small gels are probably transformed into larger networks by local reorganization [6].

In the end of the process, the main product of reaction is called alkaline alumino-silicate gel (-Si-O-Al-O-). OH^- ion acts as a reaction catalyst during the activation process and Na^+ acts as a structure-forming element. The structure contains Si and Al tetrahedral

which distribute randomly along polymeric chains and also achieve charge balance for those sodium ions that correspond to the definition claimed by Davidovits.

There are some factors will influence the compressive strength of geopolymer. One of them is the ratio of Na_2SiO_3/NaOH. For Na_2SiO_3/NaOH ratio = 1.0 [7], the compressive strength can up to 70 MPa. For Na_2SiO_3/NaOH ratio = 2.5, the compressive strength drops down to 56.8 MPa [8]. Another factor is the concentration of alkaline solution. The range of concentration of NaOH solution can be used from 8 M to 16 M [9]. For concentration of NaOH solution = 6 M, the compressive strength is 40 MPa. For concentration = 12 M, the compressive strength is as high as 94.59 MPa whereas keep increasing the concentration at this point will decrease the compressive strength. While concentration = 16 M, the compressive strength drops back to 40 MPa. Keep increasing the concentration of NaOH solution will come out a negative result for strength increasing purpose [10]. The other factor could infect the compressive strength is the dry heat-curing time and it will be tested for 1, 2, 3, 6 and 24 hours under a constant temperature 60 ºC and addressed in the later experiment.

1.4 Objectives and Outlines

The main goal of this research is to design new fiber reinforced geopolymer materials with a “non-brittle” behavior, and understand its durability performance under various loading and environmental conditions. To achieve this goal, the objectives are:

1 Design new fiber reinforced geopolymer composite materials (FGC) featuring a pseudo-strain-hardening and multiple micro-cracking behavior under uniaxial tension. The FGC material design is based micromechanics theory that links fiber, matrix and

interfacial parameters with steady-state cracking criteria to achieve large tensile strain capacity of the brittle-matrix composite material.

2 Process the new FGC in laboratory conditions to achieve the designed material properties. Understand how the curing conditions influence the tensile behavior of FGC.

3 Evaluate the elevated temperature effects (up to 600 °C) on FGC.

4 Elucidate the behavior of FGC under drying shrinkage conditions, and how the fly ash/slag ratio will affect the drying shrinkage strain of FGC.

5 Measure the behavior of FGC subjected to alkali-silica reaction.

6 Measure the water permeability of FGC.

7 Characterize the corrosion resistance of FGC through accelerated corrosion tests.

This thesis is divided into five chapters. Chapter 1 includes the introduction of geopolymer materials, the motivation and objectives of this research, and literature review of the past relevant work. Chapter 2 describes the theoretical framework for designing the FGC with ductile strain-hardening behavior. It also summarizes the mechanical properties of newly designed FGC. Chapter 3-7 focus on characterizing the durability aspects of the newly designed FGC, including elevated temperature effects, drying shrinkage, alkali-silica reaction, water permeability and corrosion of embedded steel. Chapter 8 concludes the study and suggests future work.

CHAPTER 2: DESIGN OF DUCTILE GEOPOLYMER

2.1 Material Design Framework

This “non-brittle design theory is based on micromechanics and it has been developed in the early 1990’s [60, 61]. The way to achieve strain-hardening performance in a brittle material is to increase its toughness. Mix numbers of fibers into the brittle matrix is a useful way to enhance the strain capacity of the composite. The strain hardening behavior is associated with the multiple cracking phenomenons generated on the matrix. Those multiple cracks are bridged by the numbers of fibers to against further crack propagation, thus increase the strain capacity.

The theory links to three different levels of scales: micro-scale, meso-scale and macro-scale. For micro-scale level, this part of theory focuses on measurable micro-scale constituent parameters that are the behavior between single fiber and matrix. For meso-scale level, analysis the behavior of single crack with numbers of fibers bridging the matrix. In the macro-scale level, combine multiple cracks perform on the designed material to achieve strain-hardening behavior.

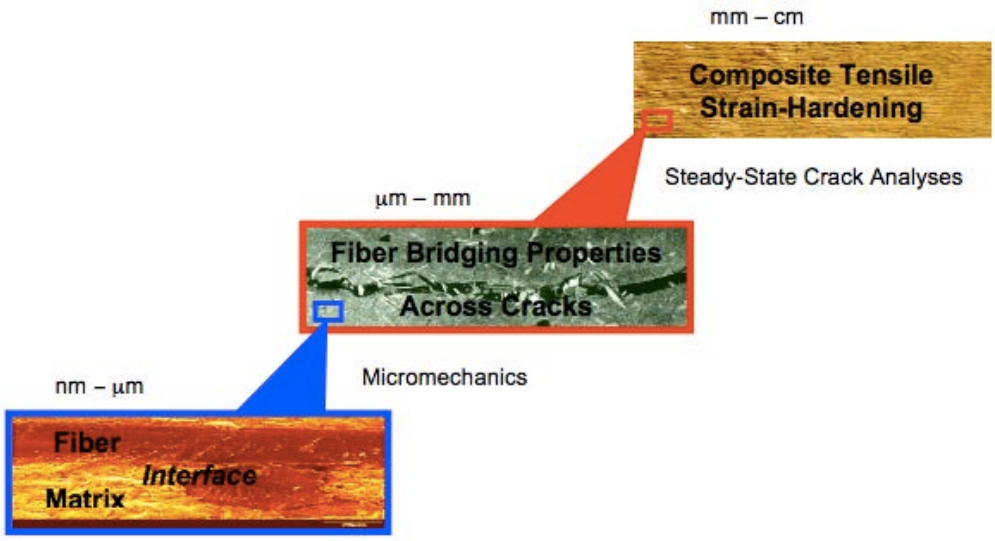

Figure 2.1: Scale Linking in Development of Strain-hardening Composite [62]

2.1.1 Micro-scale: Single Fiber Debonding and Pull-out Behavior

The behavior of embedded single fiber pulled-out from the matrix can be divided to two stages [64]: (1) Fiber Debonding Process, and (2) Fiber Pull-Out Process that the relation of force and displacement can be plotted on the p-u curve (Figure 2.1).

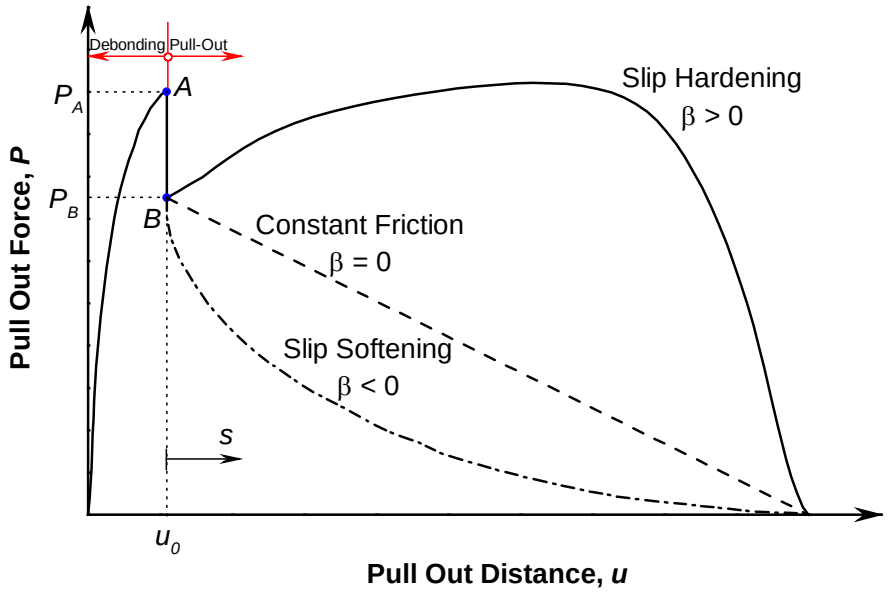

Figure 2.1: General profile of a single fiber pull-out curve [63]

(1) Fiber Debonding Process:

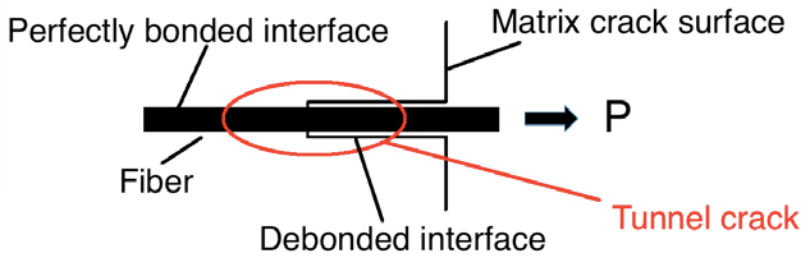

Figure 2.2: Schematic illustration of fiber debonding behavior

The stress of the fiber debonding process can be computed by equation (2.1)

$$\sigma = 2\sqrt{(\tau_0 u + G_d)\frac{2E_f(1+\eta)}{d_f}}, \tag{2.1}$$

where, d_f is the diameter of fiber, τ_0 is the frictional bond strength of fiber/matrix interface, u is the displacement from the free end of the fiber to the crack surface, G_d is chemical debonding energy of fiber/matrix interface, and E_f is Young's modulus of fiber. The frictional bond strength is,

$$\tau_0 = \frac{P}{\pi d_f L_e}, \tag{2.2}$$

where, L_e is the fiber embedded length. Besides,

$$\eta = \frac{E_f V_f}{E_m(1-V_f)}, \tag{2.3}$$

where, V_f is the volume fraction of fiber and E_m is Young's modulus of matrix. The displacement discontinuity at the free end of the fiber is

$$u = \delta_t(a) = \frac{\sigma a}{E_f} - \frac{2\tau_0 a^2}{E_f d_f}(1+\eta)\,, \tag{2.4}$$

where, a is the length of tunnel crack. The maximum stress and displacement of fiber debonding process can be obtained from equation (2.5) and (2.6)

$$u_0 = \frac{2\tau_0 L_e^2(1+\eta)}{E_f d_f} + \frac{L_e}{E_f}\sqrt{\frac{8G_d E_f(1+\eta)}{d_f}} \tag{2.5}$$

and

$$\sigma_0 = \frac{4\tau_0 L_e(1+\eta)}{d_f} + \sqrt{\frac{8G_d E_f(1+\eta)}{d_f}}. \tag{2.6}$$

(2) Fiber Pull-out Process:

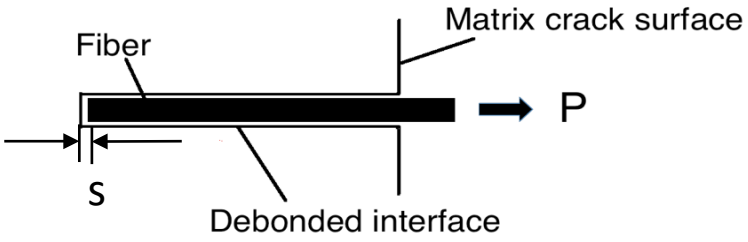

Figure 2.3: Schematic illustration of fiber pull-out after complete debonding

The force of the fiber pull-out process can be computed by equation (2.7)

$$\sigma = \frac{4\tau_0}{d_f}(L_e + u_0 - u)\left(1 + \beta_1 \frac{u - u_0}{d_f} + \beta_2 \frac{(u - u_0)^2}{d_f^2}\right), \quad (2.7)$$

where, $\beta_1$and β_2 are the slip hardening property between the interface of fiber and matrix. Fiber displacement relative to the crack surface (u) is

$$u = s + u_0 \, . \quad (2.8)$$

Equation (2.1) and (2.7) are rearranged to Equation (2.9) & (2.10) that sum the expressions for the debonding and pull-out process$(P - u)$.

For $u \leq u_0$,

$$P = \frac{1}{2}\pi d_f^2 \sqrt{(\tau_0 u + G_d)\frac{2E_f(1+\eta)}{d_f}} \, . \quad (2.9)$$

For, $u \geq u_0$,

$$P = \pi d_f \tau_0 (L_e + u_0 - u)\left(1 + \beta_1 \frac{u - u_0}{d_f} + \beta_2 \frac{(u - u_0)^2}{d_f^2}\right). \quad (2.10)$$

2.1.2 Meso-scale: Single-Crack Fiber Bridging Spring Law

When focus a single crack plan, the multiple fibers bridging behavior should be considered. The relation between the single fiber pull-out force (P) and the crack opening (δ) can be expressed in a functional form (2.10)

$$P = P(\delta; L_e, d_f, G_d, \tau_0, \beta_1, \beta_2)\,. \tag{2.10}$$

Each single fiber bridging force was given by equation (2.11) to (2.13).

For $0 \le \delta \le \delta_0$,

$$P(\delta) = \sqrt{\frac{\pi^2 \tau_0 E_f d_f^3 (1+\eta)}{4}\delta + \frac{\pi^2 G_d E_f d_f^3 (1+\eta)}{2}}. \tag{2.11}$$

For $\delta_0 \le \delta \le \delta_0 + L_e$,

$$P(\delta) = \pi d_f \tau_0 (L_e - \delta + \delta_0)\left(1 + \beta_1 \frac{\delta - \delta_0}{d_f} + \beta_2 \frac{(\delta - \delta_0)^2}{d_f^2}\right). \tag{2.12}$$

For $\delta_0 + L_e < \delta$,

$$P(\delta) = 0\,. \tag{2.13}$$

Equation (2.11)-(2.13) only expresses the special case of force and displacement relation when fiber has normal orientation that perpendicular to crack plan without any inclination ($\phi = 0$) (Figure 2.4). However, in general case, fibers are randomly dispersed in the matrix. Each single crack is bridged by numbers of fibers and each fiber has different embedded length and inclination angle (Figure 2.5). Thus, in order to compute the

complete stress applied on the crack, both of the parameters fiber embedded length (L_e) and the inclination angle (ϕ) should be taken into concern.

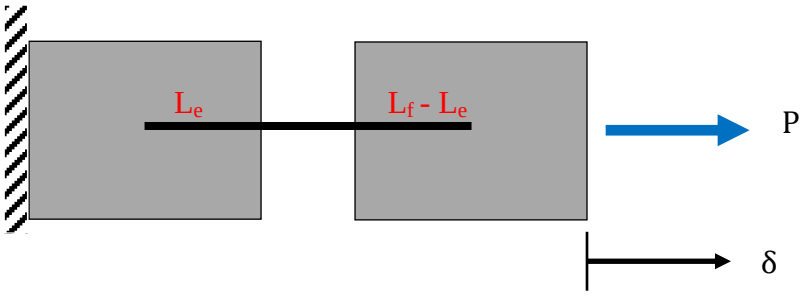

Figure 2.4: Crack bridging fiber, $P(L_e, \delta)|_{\emptyset=0}$

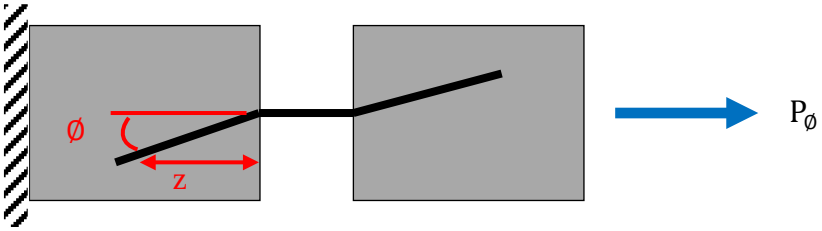

Figure 2.5: Crack bridging fiber with inclination angle, $P(L_e, \emptyset, \delta)$

The numbers of fibers bridging across the matrix crack plane should be considered either. The summation about the composite bridging stress-crack opening relation can be expressed in equation (2.14) which

$$\sigma(\delta) = \frac{4V_f}{\pi d_f^2} \int_{\emptyset 0}^{\emptyset 1} \int_{z=0}^{\frac{L_f}{2}\cos\emptyset} P(L_e, \delta)|_{\emptyset=0} e^{f\emptyset} p(\emptyset) p(z) dz d\emptyset \,, \qquad (2.14)$$

where, $p(\phi)$ is the probably density function for random fiber orientation and p(z) is the probably density function for randomness of centroidal distance.

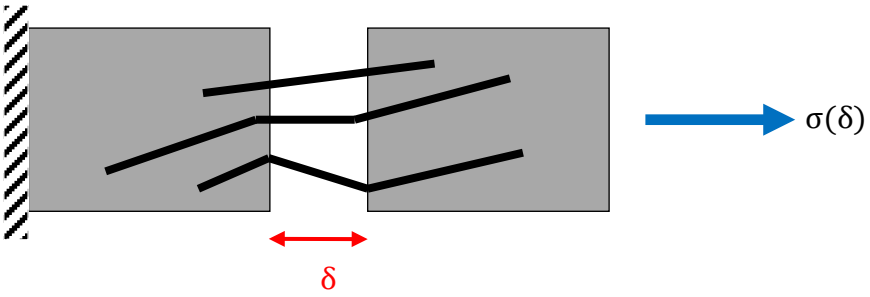

Figure 2.6: Composite bridging stress-crack opening

2.1.3 Macro-scale: Composite Strain-hardening Behavior

Figure 2.7 shows the various size and distribution of flaws in strain-hardening material. When the tensile load is applied the first crack develops corresponding to the weakest section. It is corresponding to largest flaw. The activated first crack is bridged by the spring-like fibers. The cracks section can resist further load. Then, the second crack develops corresponding to the next weakest section. It is corresponding to the second largest flaw. The crack is bridged and can resist more loads. The similar phenomenon occurs several times to develop several controlled stable cracks until the required force is larger than fiber bridging capacity, then the material fails at the weakest section.

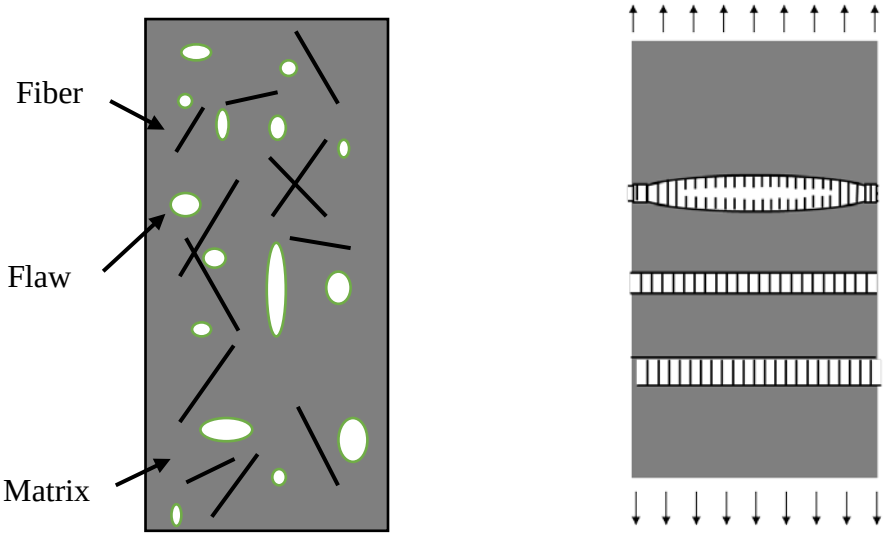

Figure 2.7: Schematic Illustration of fiber composite with multiple cracking

2.1.4 Strain-Hardening Criteria

The tensile strain-hardening behavior of the non-brittle cementitious composites can be approached through the formation of multiple cracks on the matrix. These tight cracks are bridged by fibers that randomly distribute in the matrix. The cracks are designed to be generated as a steady state flat crack rather than Griffith type crack (Figure 2.8). For Griffith type cracks, they are oval shape crack with a descending ambient load and a widened crack opening when applying ambient load. This kind of crack will lead to localize fracture and it cannot achieve strain-hardening behavior. On the other hand, steady state cracks are flat in shape with constant ambient load and constant crack opening. The extension of a matrix crack is accompanied by fiber bridging across the crack flanks. This type of crack can achieve multiple cracks on the matrix to satisfy the strain-hardening criteria then achieve ductile behavior. In order to have steady state cracks on the matrix, material need to satisfy two criteria by energy and strength [61].

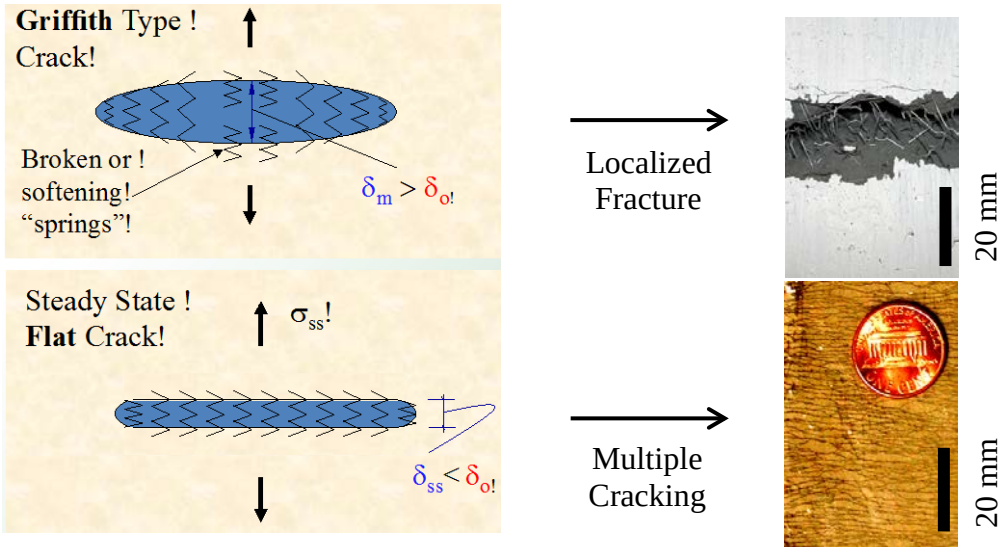

Figure 2.8: Griffith type crack & steady-state flat crack have different failure mode

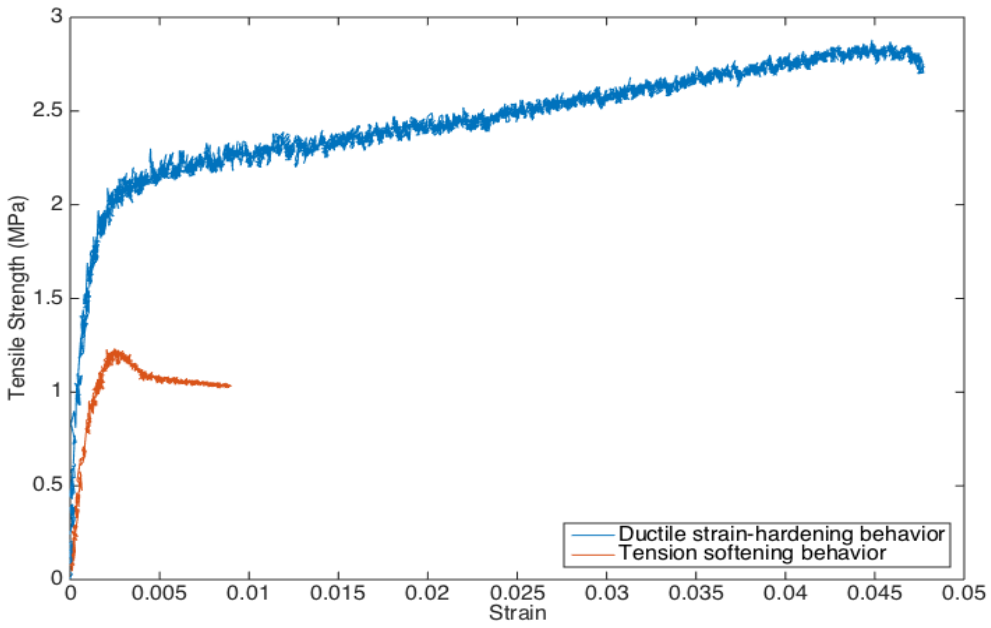

Figure 2.9: Tension softening behavior by localized fracture & ductile strain-hardening behavior by multiple cracking

(1) Energy Criterion:

Energy criterion is the first condition. To ensure having steady-state flat crack, the crack tip energy (J_{tip}) must be less than the complementary energy (J_b') which shown in equation (2.15)

$$J_{tip} \leq \sigma_0 \delta_0 - \int_0^{\delta_0} \sigma(\delta) d\delta \equiv J_b' \,. \tag{2.15}$$

J_b' is the crack driving energy which can be estimated by the function of fiber bridging relation σ(δ) equation (2.14). J_{tip} can be approximated to fracuture energy release rate in

brittle matrix (G_m) which can be computed by the fracture toughness (K_m) and Young's modulus (E_m) which shown as equation (2.16).

$$J_{tip} \cong G_m = \frac{K_m^2}{E_m}, \tag{2.16}$$

where, J_{tip} = Crack tip toughness, $J_b^{'}$ = Complementary energy, σ = Fiber bridging stress, δ = Crack opening, σ_0 = Maximum fiber bridging stress corresponding to δ_0, G_m = Matrix fracture energy release rate, K_m = Matrix fracture toughness, E_m = Matrix Young's modulus

(2) Strength Criterion:

Another condition is required the driving force for crack propagation on the matrix must less than the fiber bridging capacity ($\min[\sigma_0]$) which shown in equation (2.17)

$$\sigma_{ss} = \sigma_{ci} \leq min[\sigma_0], \tag{2.17}$$

where, σ_{ci} = Matrix tensile crack initiation stress, σ_0 = Maximum fiber bridging stress corresponding to δ_0, σ_{ss} = Steady state cracking stress. As the result, matrix can generate multiple cracks before the embedded fiber rupture.

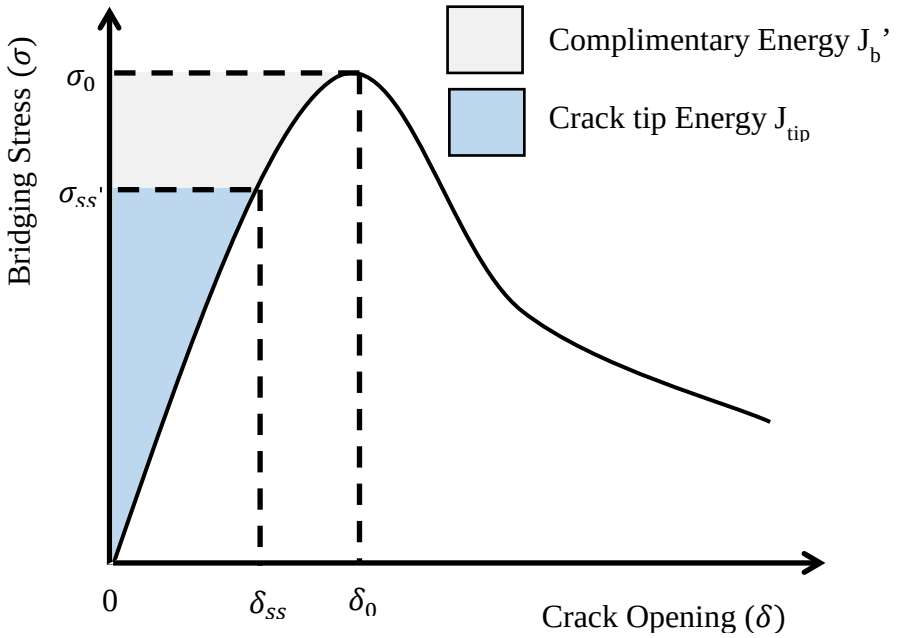

Figure 2.10: Crack bridging stress & crack opening relation for strain-hardening composite

2.2 Material Ingredients and Processing

In this research, low-calcium (ASTM C618 class F) dry fly ash (FA) and blast furnace slag (Slag) were selected to use as the base materials for producing strain-hardening fiber geopolymer composites. FA is the main material for geopolymerization which is commercially available from Boral limited, USA. The composition on ingredients of FA is presented in Table 2.1. Slag is used for the purpose of increasing the strength of structure in a short period which is commercially available from Holcim (US) Inc. The alkali activator is a mixture solution which mixed by sodium silicate (Na_2SiO_3) and sodium hydroxide (NaOH). Na_2SiO_3 consisting of Na_2O = 9%, SiO_2 = 28%, and H_2O = 63% at a specific gravity of 20ºC (68ºF). This sodium silicate solution is commercially available from The Science Company. NaOH is in pellet form with more than 98% purity which is also commercially available from Avantor Performance Materials, Inc.

Whether or not geopolymer mortar has good mechanical properties and moderate setting time were first determined by the mix proportion. According to Davidovits and some publish papers [4, 5, 10]. The weight ratio of FA and Slag to alkaline activator was selected to fix as 3.2 for sodium alkaline solution. To prepare NaOH solution, the concentration of the solution was used 16.7 molarities (M) and the NaOH pellets were dissolved in de-ion water. Besides, use the weight ratio 2.3 of Na_2SiO_3/ NaOH in order to achieve good strength. The mixing proportion of FGC and control mortar is shown in Table 2.2. The alkaline activate solution consisting of mixture Na_2SiO_3 and NaOH solution was prepared at least 24 hours before casting to make sure the solution has been completely reacted. Dry mixing FA and Slag about three minutes until they were homogeneously blended with each other before pouring into alkaline activator. Continue the stirring process until it appeared a uniform state then continually added fine silica sand and extra de-ion water which was for increasing workability and keep stirring for another three minutes. As long as the mixture state became viscous, speeding up the mixer and start adding polyvinyl alcohol (PVA) fibers (Table 2.3) to ensure the fiber can be well dispersed for the last three minutes.

All of the casting was done on the vibration table to avoid pores formed by inhomogeneous casting. Immediately after casting, FGC were poured into each mold and covered by a film to prevent the loss of water due to evaporation while during dry heat-curing which cured the specimens under an elevated temperature. Specimens of FGC were cured in an oven at a selected temperature, 60 ºC for the next 24 hours after casting to approach the same compressive strength condition as other control specimens. At the end of curing period, removed specimens from the mold and kept them in the plastic bag

for 7 days to avoid a dramatic change of the environmental conditions. Furthermore, Control mortar specimens were prepared undergoes the ordinary casting procedure and cured at 65 ± 5% RH and 25 ± 1 ºC environment for 28 days. The specimens were ready for each test after foregoing processes.

Table 2.1: Composition of Class F fly ash

Substance	**Percentage (%)**
Alumino-silicates (Al_2SiO_5)	40-100%
Silica (SiO_2)	< 4.0%
Calcium oxide (CaO)	< 20%
Potassium oxide (K_2O)	< 5 %

Table 2.2: Mixing proportion of FGC and control mortar by weight ratio

Substance	**FGC**	**Mortar**
Fly Ash (Type F)	8	-
Slag	2	-
Sand	3.5	0.43
Sodium Silicate Solution	2.5	-
Sodium Hydroxide Solution	1	-
Water	0.2	1.3
Fiber, V_f (%)	2	-
Cement	-	1

Table 2.3: Properties of PVA fibers

Fiber type	Poly-Vinyl Alcohol
Nominal strength (MPa)	1620
Apparent strength (MPa)	1092
Diameter (μm)	39
Length (mm)	12
Young's modulus (GPa)	42.8
Elongation (%)	6.0

2.3 Mechanical Properties

Mechanical properties of prepared specimens were tested 7 days after dry heat-curing period. For each group of different dry heat-curing period were tested to understand their capability of compressive and tensile strength. Each group contained three cylinder specimens and three coupon specimens were subjected to uniaxial compression and tension test. For each cylinder compressive specimen, the size was 50.8 mm (2 inches) for diameter and 101.6 mm (4 inches) for height. For each tensile coupon specimen, the size was 305 mm (12 inches) for the length, 76.2 mm (3 inches) for the width and 12.7 mm (0.5 inches) for thickness.

2.3.1 Uniaxial Compression

The uniaxial compressive test of both FGC and control mortar specimens was conducted by closed loop Tinius Olsen hydraulic testing frame with 450 kips (2,000 KN) capacity. This testing procedure of uniaxial compressive test was to measuring load–displacement curves under displacement control with the rate of 0.0025 mm/s, according to ASTM C39 [48]. Tested specimens were capped on both ends since the compressive force should be uniformly distributed loading on the cross-section of the specimens for the experiment accuracy. The method used to test the uniaxial compressive strength was according to ASTM C1231 [59]. This practice covers requirement for a capping system using an unbonded caps for testing concrete cylinder specimens. An elastomer pads within the cover caps which is available in different hardness scale. Due to this unbonded capping with elastomer pads is easier than bonded capping (ASTM C617 [60]), the method of ASTM C1231 was used in later uniaxial compression test.

Different dry heat-curing time and temperature caused different strength capacity of FGC. Figure 2.13 displays different compressive strength at different dry heat-curing time, 0, 1, 2, 3, 6, and 24 hours of curing time were tested respectively. Extending the period of the curing time had significant effect to increase the compressive strength in the early age. Especially on 2 to 6 hours curing period, the compressive strength severely increased and gradually approach plateau while curing period up to 24 hours. After 24 hours dry heat-curing period, the compressive strength can achieve around 66 MPa which is good enough for construction purpose.

Figure 2.11: Uniaxial compression test with a cylinder specimen

2.3.2 Uniaxial Tension

Due to the “pseudo deflection hardening behavior” which can be seen on the tension-softening materials, the direct uniaxial tensile test is the most persuaded method for validating strain-hardening material performance. The specimens were fixed by the clips

with the middle gage length 102 mm (4 inches) (Figure 2.12). Both the ends of the specimens were strengthened to accurate measurement of strain. As the result of that multiple cracking only occurred in the gage length. Those tests were conducted under displacement control with the rate of 0.0025 mm/s to stimulate quasi-static loading state. Two external linear variable differential transformers (LVDTs) were attached to the surface of specimen in order to measure displacement for calculating strain.

By through uniaxial tensile test, the strain-hardening behavior can be divided into three different stages: (i) The initial elastic stage which was characterized by Young's modulus. (ii) The strain-hardening stage, this stage starts from the first crack occurred on the specimen and this starting point can be characterized as the strength when first crack forms. Multiple micro-cracking formations occurred in this stage. In spite of the number of micro-cracking keep increasing, the width of each micro-crack almost remains same. The strain-hardening behavior of the tested material performs in this stage. (iii) The tension-softening stage, this stage starts from the formation of a localized fracture which means one of the micro-crack propagates at this point. In this stage, the ambient load drops down sharply that indicates after this certain point the material loss its tensile strength capability rapidly. Figure 2.14 displays the tensile stress-strain relation of FGC specimens that with and without dry heat-curing process. Dry heat-curing can enhance the tensile strength and ductility of FGC specimens. The one without any curing only had 1.867 MPa tensile strength and 0.04% strain capacity. Another specimen with 60 ºC dry heat-curing can approach 2.737 MPa tensile strength and 0.05% strain capacity.

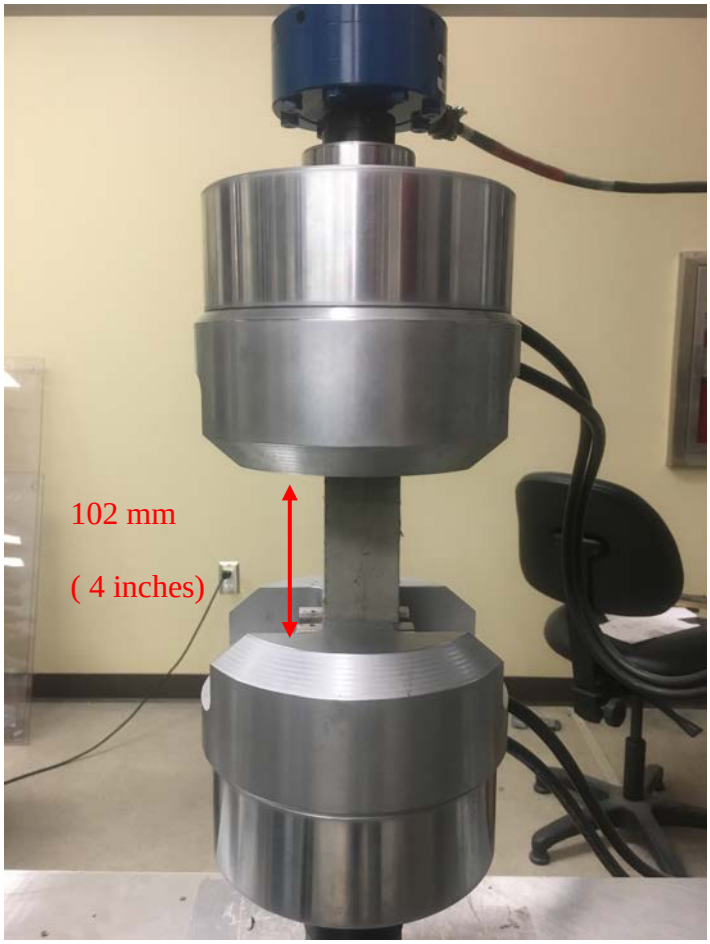

Figure 2.12: Uniaxial tension test with a coupon specimen, gage length:102 mm (4 inches)

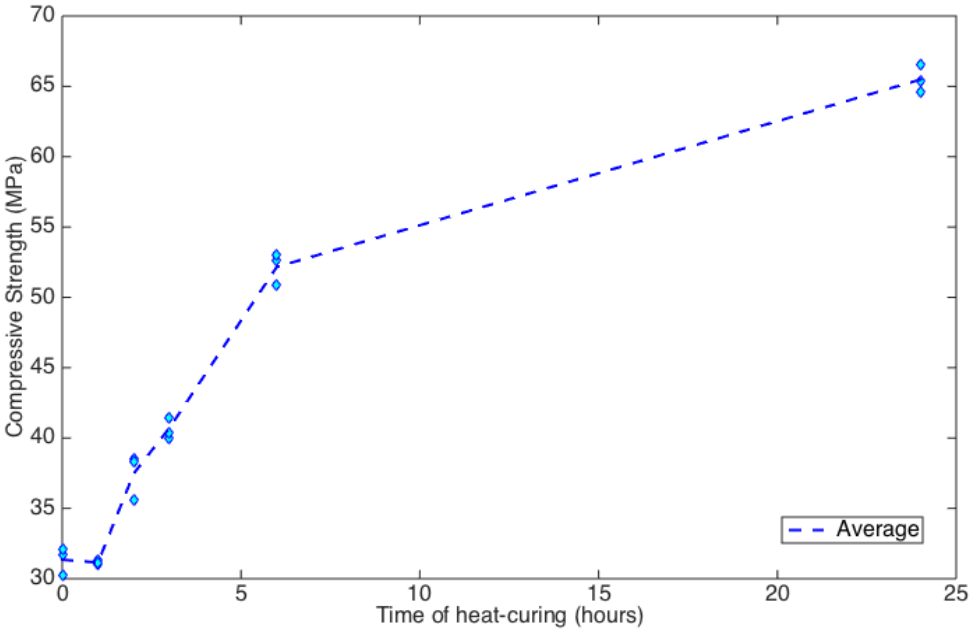

Figure 2.13: Effect of heat-curing time on compressive strength of FGC

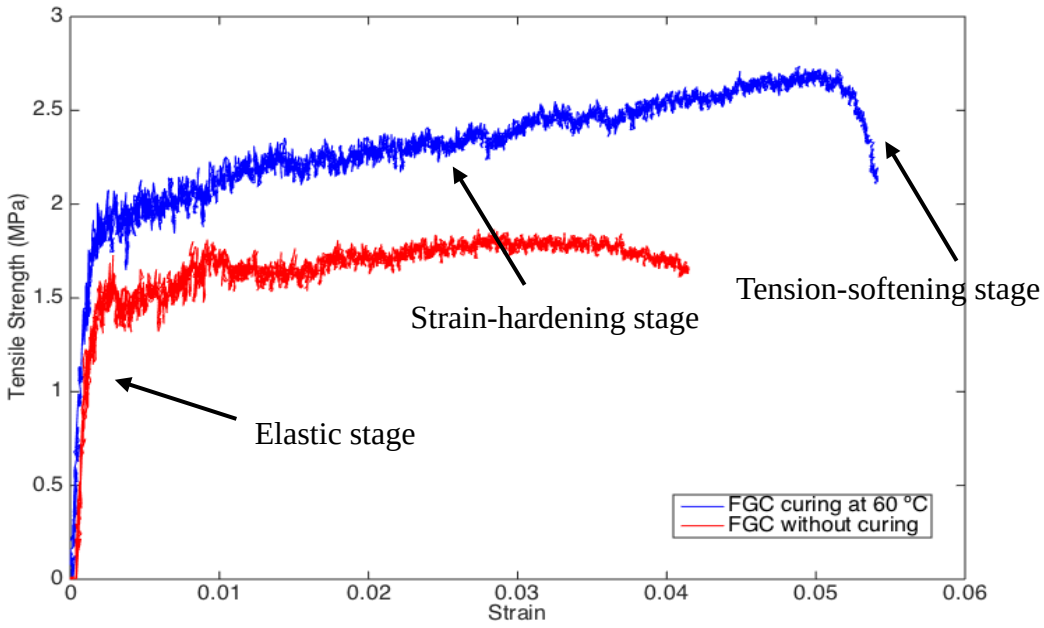

Figure 2.14: Tensile strength-strain relation of FGC with and without high temperature (60 ºC) curing

CHAPTER 3: ELEVATED TEMPERATURE EFFECT ON DUCTILE GEOPOLYMER

3.1 Introduction

When considering geopolymer concrete as a material used in industry construction applications, the performance of mechanical strength while elevating temperature should be noticed and the resistance to strength deterioration at high temperature may be expected. The comparison of thermal coefficient with OPC concrete was studied under 20-1000 ºC by Lucie et al. [11]. They claimed the thermal coefficient of geopolymer concrete was significantly lower. As the result, lower thermal stress contributed by lower thermal strain and led to lower risk of failure of structure element. Geopolymer concrete has greater thermo mechanical behavior than OPC concrete. John et al. found out that while the geopolymer specimens under temperature range from 700 to 800 ºC displayed small expansion and the best strength performance [12]. Daniel et al. presented a study that geopolymer composite samples increased about 53% strength after exposed to temperature over 800 ºC. As the result of that, increasing the temperature would increase the combination of polymerization. In their test, the aggregate steadily expanded with temperature reaching about 1.5 to 2.5% expansion at 800 ºC. The expansion caused the decline in strength [13]. Maurice et al. reported the effect of alkali-activated slag concrete (AASC) when elevated temperature exposure up to 1200 ºC. The remaining strength of AASC from 76% to 10 % while increasing the exposure temperature from 200 to 800 ºC was similar to OPC concrete. The Alkali-activate slag (AAS) paste had significant higher thermal shrinkage than other paste while the basalt aggregate expand. They believed the

dominant mechanism of deterioration in concrete specimens are thermal incompatibility between aggregate and paste, therefore it led to the strength loss of AASC at elevated temperature [14]. The behavior of geopolymer which activated by potassium (K) type of solution has also been found by Valeria et al. that had outstanding thermal stability and only showed little sign of melting up to 1400 ºC [15].

The mechanical properties study of on strain-hardening cementitious composites (SHCC) was done by Motohiro Ohno and Victor C. Li that using randomly oriented short PVA fibers to achieve great ductility [5]. The effect of tensile strength and strain capacity and compressive strength of elevated temperature on strain-hardening engineered cementitious composite material (ECC) has been discussed by Prakash et al. ECC lost its strain-hardening behavior when the temperature above 200 ºC but there was no spalling in both ECC tensile and compressive specimens even the temperature is up to 600 ºC. The spalling resistance can be contributed to tensile strength capacity and the increase in porosity due to the melting of PVA fibers [16].

Although various different thermal characteristic affected by different starting raw materials and preparation parameters, geopolymer concrete has a high potential for use in producing fire resistance structures via the optimization of the mixture design and curing conditions.

3.2 Experimental Setup

In this test, for preparing tensile specimens, the mixtures were casted into tensile coupon molds that 305 mm (12 inches) for the length, 76.2 mm (3 inches) for the width and 12.7 mm (0.5 inches) for thickness to each specimen. For compressive specimens,

the mixtures were casted into cylinder molds that 76.2 mm (3 inches) for diameter and 152.4 mm (6 inches) for height. Those molds were cover by plastic film and demolded after 24 hours. FGC specimens were dry heat-cured by the way mentioned above before demolded and mortar specimens were cured at a humidity condition.

At the end of curing period, the specimens were heated in an electric furnace with a heating rate 24.5 ºC/min for different temperature exposure. Test the temperature range from 100 ºC to 600 ºC and each interval 100 ºC did a test [16]. Control specimens were stored at a room temperature 20 ºC were not subjected to heating. While the temperature was achieved, specimens were placed under this temperature in the furnace. In order to approach steady-state thermal condition, there was 2 hours heating period for tensile specimens and 6 hours heating period for compressive specimens. Those specimens were then test in direct uniaxial tension and uniaxial compression under room temperature.

3.3 Experimental Results

3.3.1 Mass Loss

Table 3.1 & Table 3.2 and Figure 3.1 summarize the percentage of mass loss of the compressive specimens after different heating condition. The mass loss was rapidly between 200 ºC to 400 ºC, and approached to plateau while the temperature was higher than 400 ºC. The detail results of the average percentage of mass loss were 4.81%, 9.01%, 10.5%, 12.3%, 12.47% and 12.47% of the specimens that under 100 ºC, 200 ºC, 300 ºC, 400 ºC, 500 ºC and 600 ºC, respectively. The mass loss can not only be associated with the moisture loss in the specimens that water which existed in large pores

and small capillary pores evaporated by elevating temperature, but also the combine water in C-S-H gel [16]. During the process of evaporation, the high vapor pressure due to rapid loss of water which attached on the surface of concrete paste caused surface cracking or even spalling. However, though the high amount of mass loss, no spalling or visual cracking was observed on FGC specimens, even those specimens that exposed under the maximum temperature of 600 ºC.

Table 3.1: Mass loss of FGC after being subjected to elevated temperatures

Sample label #	Temperature (ºC) for 6 h	Mass loss (%)	Avg. mass loss (%)
1	20 ºC	0.00	0.00
2		0.00	
3		0.00	
4	100 ºC	4.72	4.81
5		4.88	
6		4.83	
7	200 ºC	8.80	9.01
8		9.31	
9		8.92	
10	300 ºC	10.2	10.5
11		10.7	
12		10.6	
13	400 ºC	11.9	12.3
14		12.3	
15		12.7	
16	500 ºC	12.6	12.47
17		12.5	
18		12.3	
19	600 ºC	12.6	12.47
20		12.3	
21		12.5	

Table 3.2: Mass loss of mortar after being subjected to elevated temperatures

Sample label #	Temperature (ºC) for 6 h	Mass loss (%)	Avg. mass loss (%)
1	20 ºC	0.00	0.00
2		0.00	
3		0.00	

Table 3.2 continued

4	100 ºC	3.475	3.437
5		3.429	
6		3.407	
7	200 ºC	9.058	8.953
8		9.078	
9		8.723	
10	300 ºC	11.546	11.618
11		11.443	
12		11.866	
13	400 ºC	12.392	12.492
14		12.476	
15		12.608	
16	600 ºC	-	Spalling
17		-	
18		-	

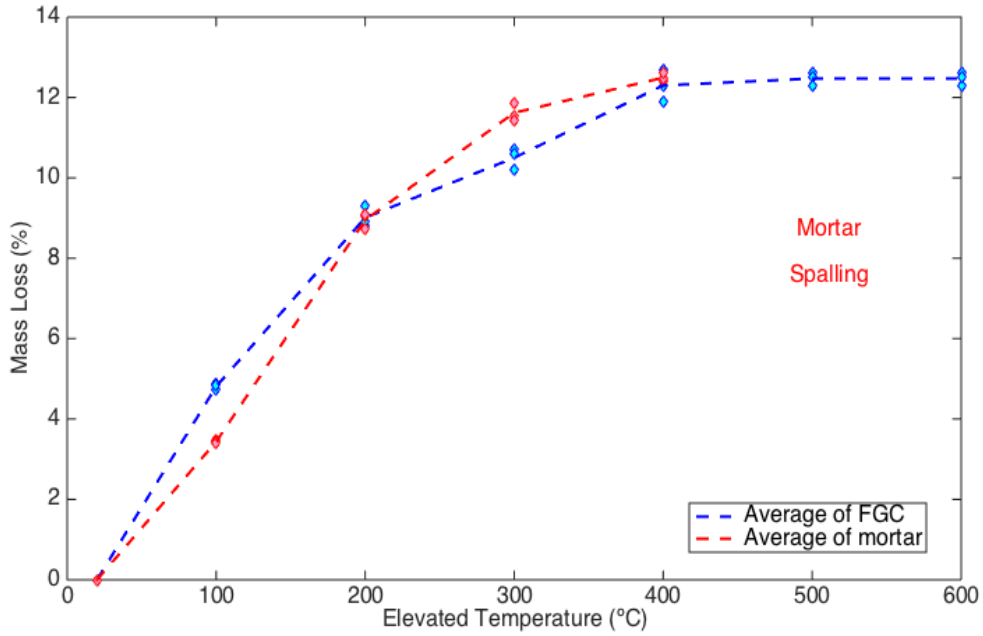

Figure 3.1: Mass loss of FGC and mortar compressive specimens

3.3.2 Effect of Elevated Temperatures on FGC Compressive Strength

Spalling was occurred on the control specimens, mortar after 30 to 75 minutes of exposure to the maximum temperature of 600 ºC. The spalling was explosive as shown in

Figure 3.2 & Figure 3.3. Comparing mortar with FGC, though the maximum mass loss almost approached 12% of both materials, there was no spalling or visible degradation on the surface observed on FGC. The result of the compressive test of elevated temperature was shown in Figure 3.4. The compressive strength capacity of FGC increased from approximately 60 MPa to 80 MPa while the temperature increased to 100 ºC. However, sustain increasing temperature led to lower compressive strength than usual. After exposing less than 600 ºC for 6 hours, FGC specimen remained only 39% compressive strength.

Figure 3.2: FGC compressive specimens after 6-h exposure at 600 ºC

Figure 3.3: Mortar compressive specimens after 6-h exposure at 600 ºC

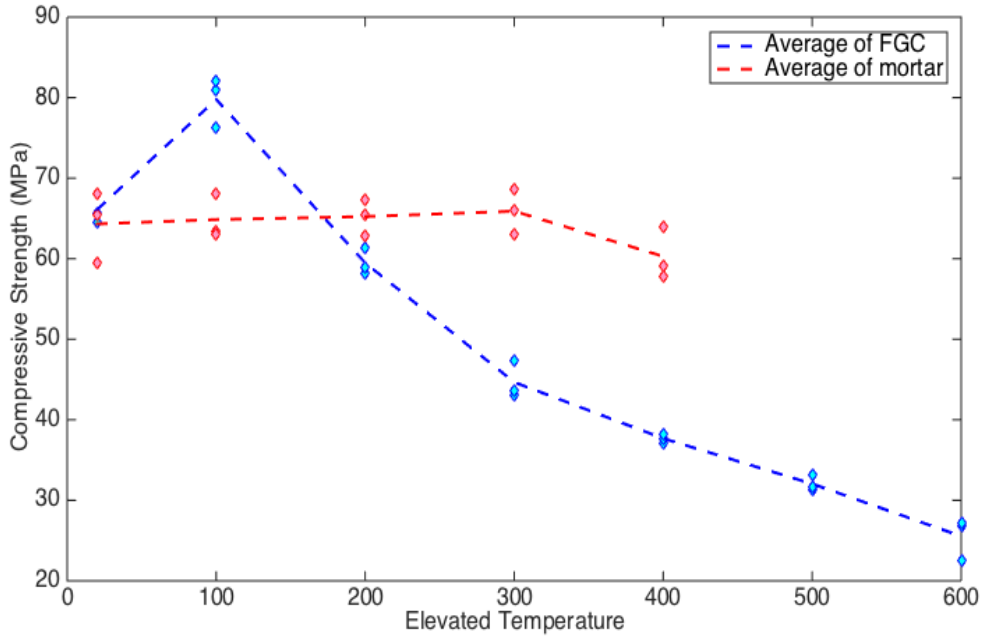

Figure 3.4: Compressive strength of FGC and mortar under elevated temperature

3.3.3 Effect of Elevated Temperatures on FGC Tensile Properties

The coupon specimens exposed to various degree of temperature were subjected to the uniaxial tension test. The tensile-strain relations were plotted on Figure 3.5 - Figure

3.8. FGC specimens had an obvious tendency of reduction of the tensile strain-hardening stage. At 20 ºC, all three specimens had the tensile strain-hardening behavior with strain capacity up to 5% and the tensile strength between 2 to 3 MPa. At 100 ºC, the tensile strength slightly rose up. However, the strain capacity of specimens reduced to 2.5-3.5%. At 200 ºC, strain-hardening behavior still existed in FGC. In spite of the tensile strain capacity was remained as the value as specimens at 100 ºC, the tensile strength further increased to more than 4 MPa. When the specimens exposed at 300 ºC or higher temperature, they lost strain-hardening behavior and almost their tensile strength capacity. They performed like a brittle material and did not exhibit any strain-hardening behavior.

The tensile strength performance of FGC is summarized in Figure 3.9 & Figure 3.10. From 20 ºC to 200 ºC, the tensile strength increased 28% on average. Lower temperature could enhance the tensile strength capacity. However, while the specimens at 300 ºC, the tensile strength decreased 90% on average. For those specimens exposed at 400 ºC or above, the material lost all of the tensile strength capacity that they were too brittle to test. It can be explained while the temperature over 300 ºC, it has been already over the melting point of PVA fiber. As the result, the rapid decomposition and pyrolysis occurred on PVA fibers. Once the material lost all of the PVA fibers, it lost the tensile strain capacity.

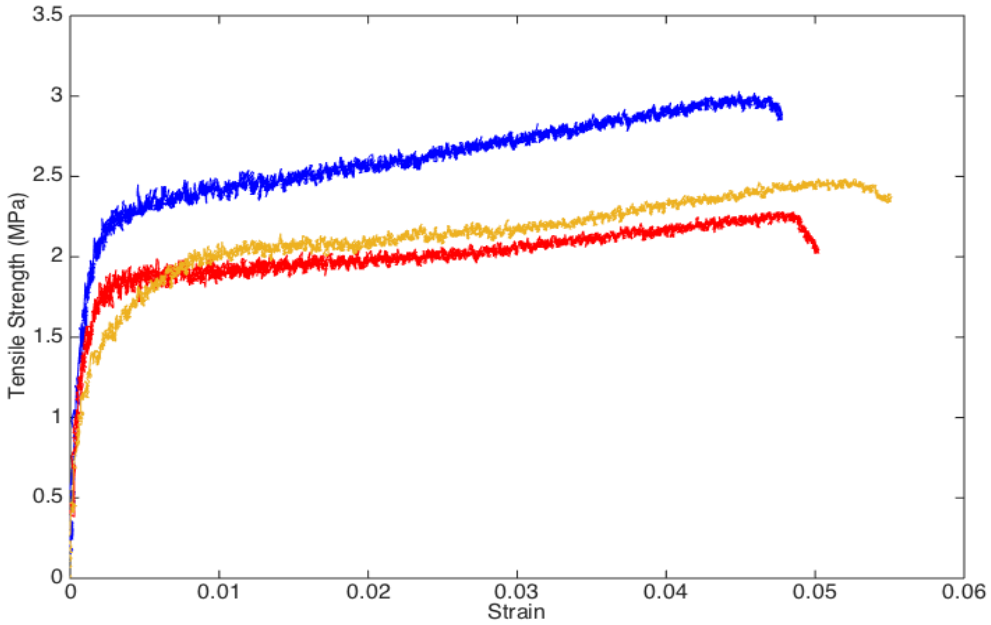

Figure 3.5: FGC tensile stress-strain relation at 20 °C

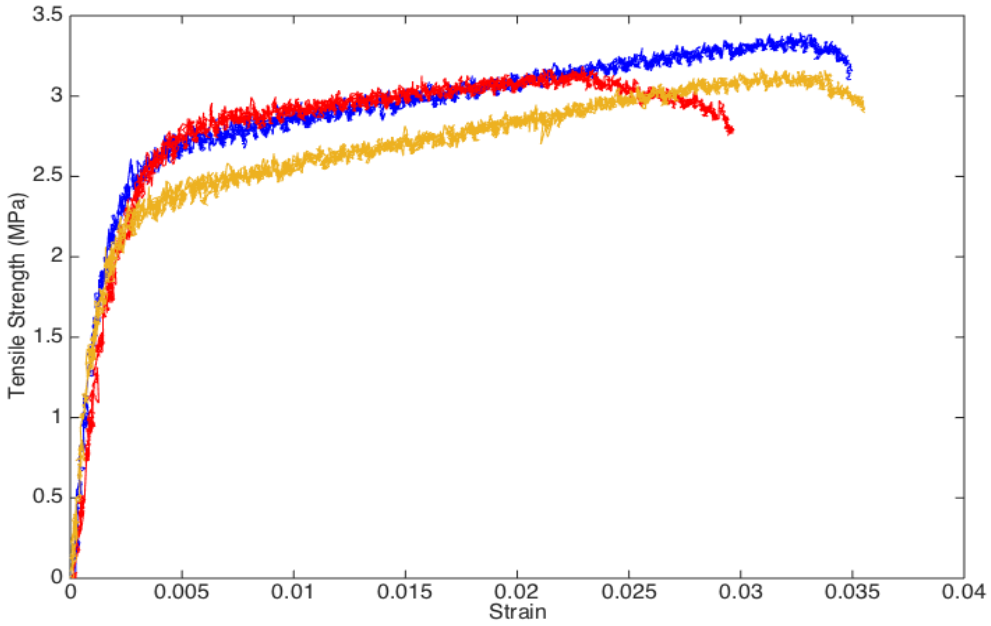

Figure 3.6: FGC tensile stress-strain relation at 100 °C

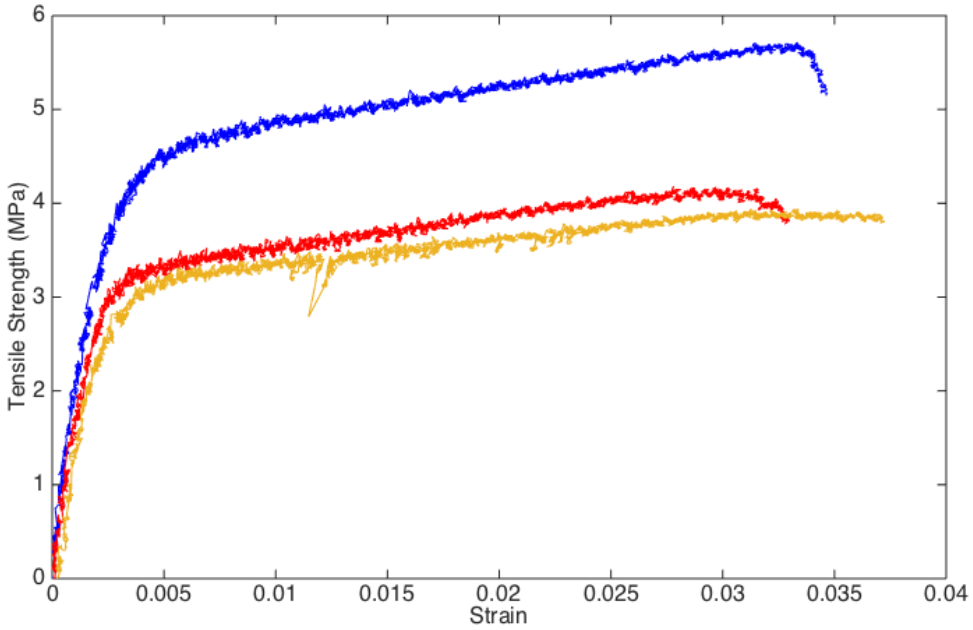

Figure 3.7: FGC tensile stress-strain relation at 200 °C

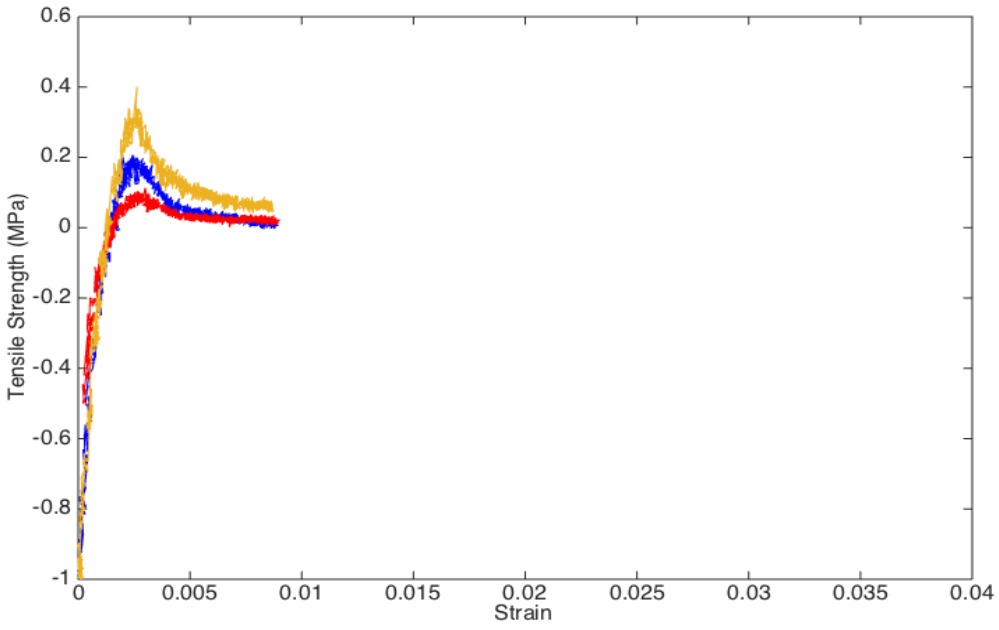

Figure 3.8: FGC tensile stress-strain relation at 300 °C

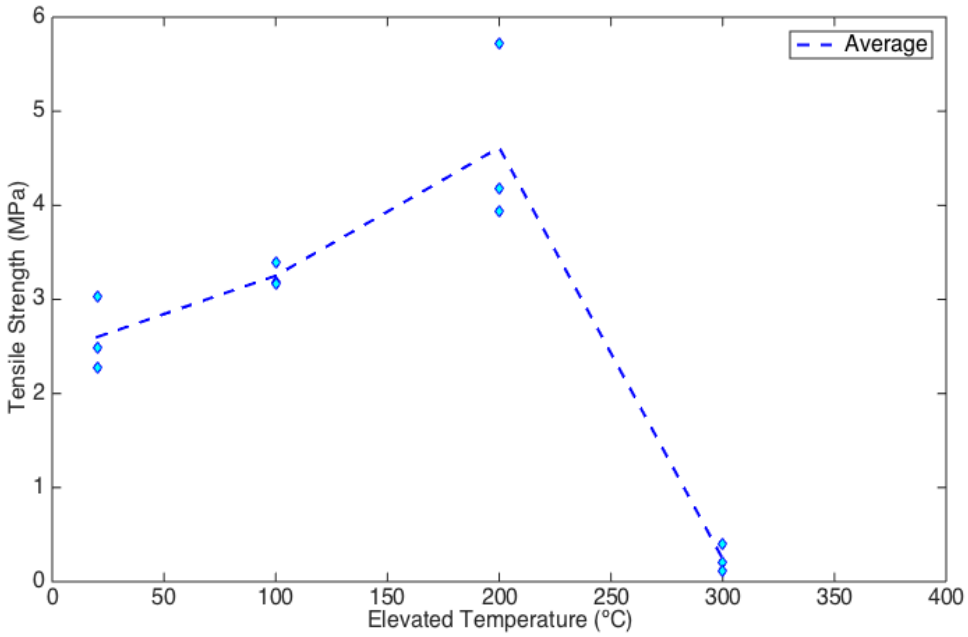

Figure 3.9: Effect of elevated temperatures on the tensile strength of FGC

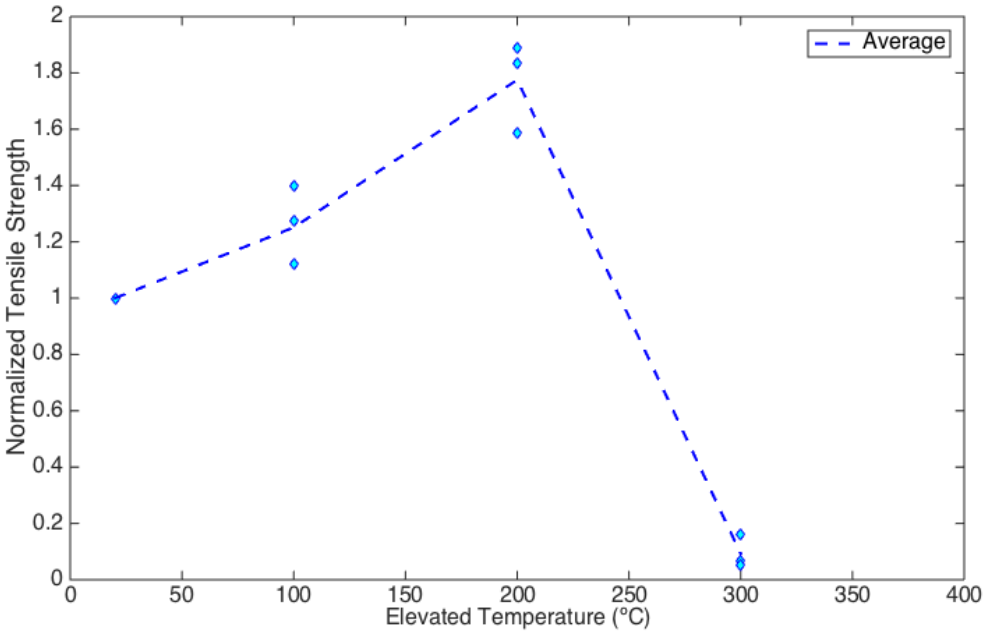

Figure 3.10: Effect of elevated temperatures on the relative tensile strength of FGC

3.4 Discussion

The compressive failure modes are shown in Figure 3.11. Those FGC and control mortar specimens were subjected to preserve at the temperature 20ºC, 100ºC, 200ºC and 400 ºC for 6 hours. Different compressive failure modes were observed on each specimen that was under different temperature condition. FGC specimens exhibited a ductile failure mode. The angle of final fracture plane was different between 20-200 ºC because the fiber orientation was randomly distributed in FGC specimen. As long as the specimen had its ductile behavior, the specimens would not explode suddenly under the increasing load. In the contrast, despite the control mortar specimens had different failure mode with different degree of angle of the crack surface, they were all suddenly failed during the test that displayed a brittle behavior. The melting point of PVA fiber is around 230 ºC, thus, after 400 ºC heating the specimen lost its fiber and ductility. Figure 24-d shows that the FGC specimen exposed under 400 ºC had a sudden failure with large splitting cracks and large pieces of specimens spalled off. This brittle behavior was similar to all of the control mortar specimens.

The reference compressive strength of mortar was lower than FGC and the evolution of strength at elevated temperature was also different for these two binders (Figure 3.4). For control mortar, the compressive strength rose up while the temperature heated from 100 ºC to 300 ºC for 6 hours, the variation of the compressive strength started dropped down from 400 ºC until the material spalling. Unlike the control mortar specimens, the compressive strength of FGC increased approximately 30% after heating to 100 ºC for 6 hours. However, the compressive strength started reducing after rising up the temperature from 200 ºC to 600 ºC. The reason might be attributing to the melting PVA fibers. It was observed that PVA fibers have melted when the temperature was over 200 ºC, thus then

created micro-pores and channels within FGC microstructure. The increasing micro-pores in the structure by elevated temperature led to the decreasing of compressive strength.

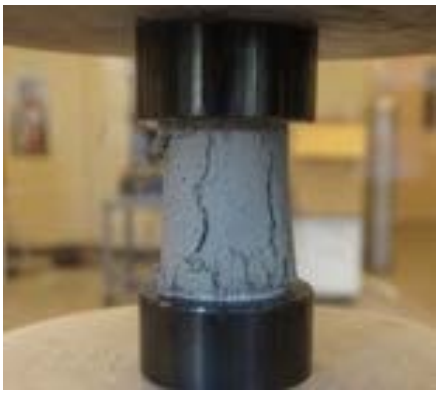

a. FGC, 20 °C

b. FGC, 100 °C for 6 hours

c. FGC, 200 °C for 6 hours

d. FGC, 400 °C for 6 hours

e. Control Mortar, 20 ºC

f. Control Mortar, 100 °C for 6 hours

g. Control Mortar, 200 °C for 6 hours

h. Control Mortar, 400 °C for 6 hours

Figure 3.11: Elevated temperature effect on the failure mode of FGC vs. control mortar compressive specimens

During uniaxial tensile test, the ambient tensile strength led to first micro-crack generated on FGC specimen. After this stage, the material went into the strain-hardening stage. In this stage, the apply load was not enough to pull the PVA fibers out from the FGC paste, but it was enough to debond the fibers between the PVA fiber surface and the concrete paste then generate another micro-crack on the material surface. As the tensile strain curve shown in Figure 3.5 - Figure 3.8, because the test is under displacement control, each tiny load drops on the curve corresponded to the formation of each micro-crack. After certain load applied on the material, PVA fibers were pulled out from the concrete paste, the micro-crack started to propagate at this point and the material lost its tensile strength capacity.

Figure 3.12 shows the side view of the final failure cross section of FGC specimens subjected to 20 ºC, 100 ºC, 200 ºC and 600 ºC for 2 hours. While the specimens were heated up to 100 ºC and 200ºC. The shape of PVA fibers seemed remains well condition as the specimens under room temperature. However, the colors became darker and darker by increasing temperature and easily broken which could explain the decreasing strain-

hardening behavior. After the temperature over 200 ºC, there were no PVA fibers observed on the fracture cross section. The FGC specimens performed like a brittle material without any strain-hardening behavior.

a. FGC, 20 °C

b. FGC, 100 °C for 2 hours

c. FGC, 200 °C for 2 hours

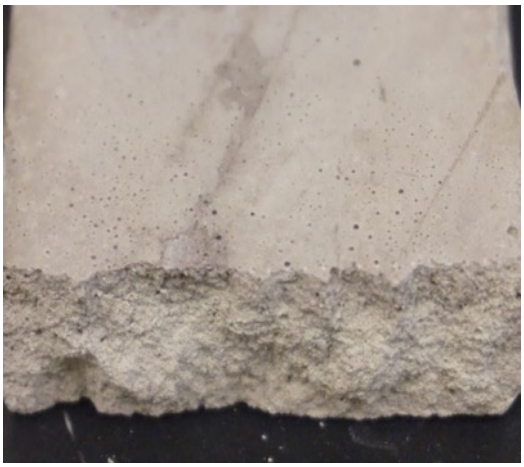

d. FGC, 600 °C for 2 hours

Figure 3.12: Side view of final failure cross section of FGC tensile specimens. It can be seen that fibers have melted when the temperature is above 200 ºC.

Scanning electron microscopy (SEM) was adopted to observe the microstructure degradation of FGC. The high-magnification SEM observations of FGC that comparing before and after elevating temperature of 600 ºC were presented in Figure 3.13. FGC material used to be dense at room temperature. However, after exposing to high temperature, the microstructure became looser as well as there appeared apparently tiny particles by degradation. Besides, a large amount of cracks was found by SEM at higher magnification after FGC specimens under 600 ºC exposures. These cracks were formed due to the expansion of fine aggregates and vapor pressure. In addition, the melting of PVA fibers within FGC specimens left pores and channels that led to ununiformed thermal expansion of aggregates that made these micro-cracks propagated more serious. This might explain while doing elevating temperature would gradually reduce the tensile strength and compressive strength.

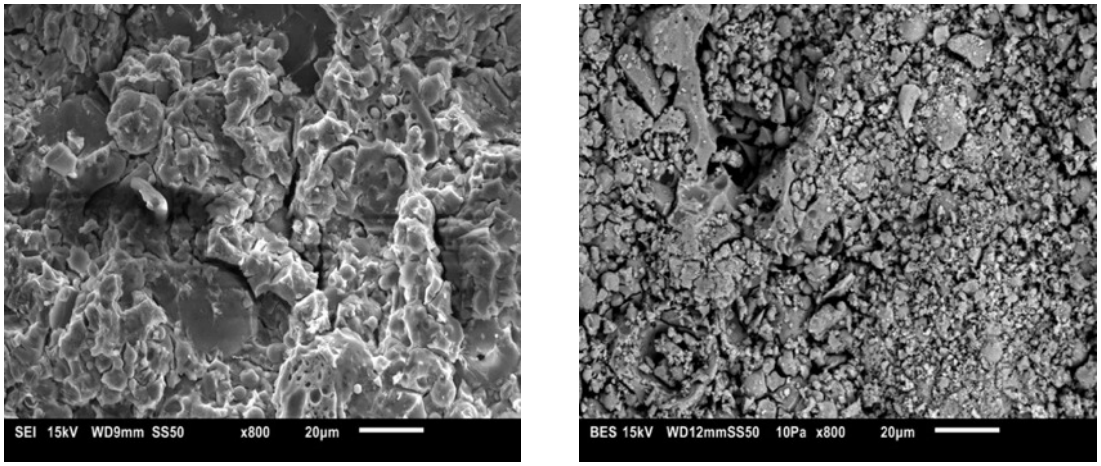

a. FGC, 20 °C b. FGC, 600 °C

Lower-magnification scanning electron microscopy of FGC

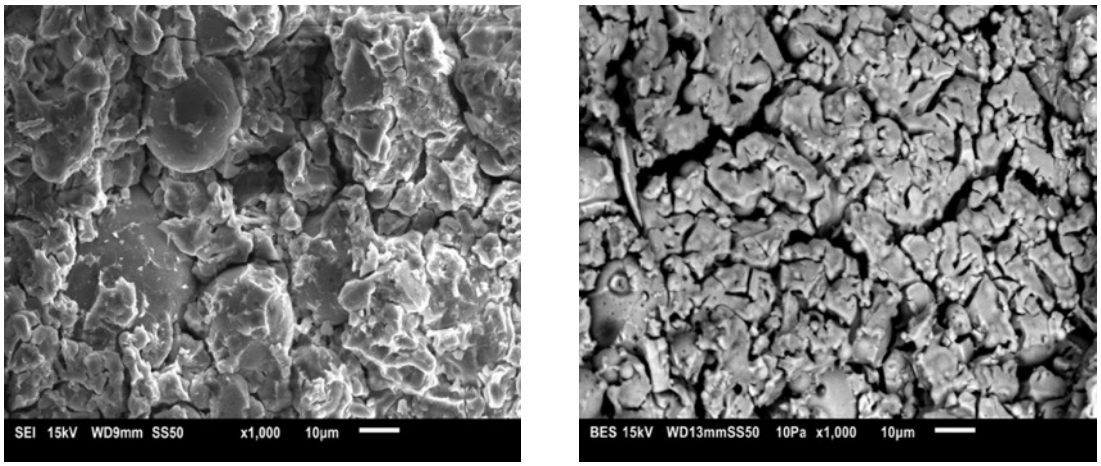

c. FGC, 20 °C d. FGC, 600 °C

higher-magnification scanning electron microscopy of FGC

Figure 3.13: SEM of FGC microstructure before and after being exposed to 600 ºC for 6 hours

CHAPTER 4: DRYING SHRINKAGE OF DUCTILE GEOPOLYMER

4.1 Introduction

All of concrete structures undergo time–dependent deformation, shrinkage. It is one of long-term property that the volume of concrete decreases with time. This phenomenon is in dependent of the external actions to concrete. Shrinkage is one of the significant factors that contribute to the cracks in structures. It is difficult to make concrete which does not shrink and crack, so the understanding of magnitude is worth be noticed. The phenomenon of shrinkage has been classified as early age and long term. Early age shrinkage takes place within a few days of casting and long term shrinkage would keep effect up to months. These two types of shrinkage behaviors can be further classified into autogenous, drying and chemical shrinkage. Erika provided a diagram of shrinkage types and stages shown in Figure 4.1 [17].

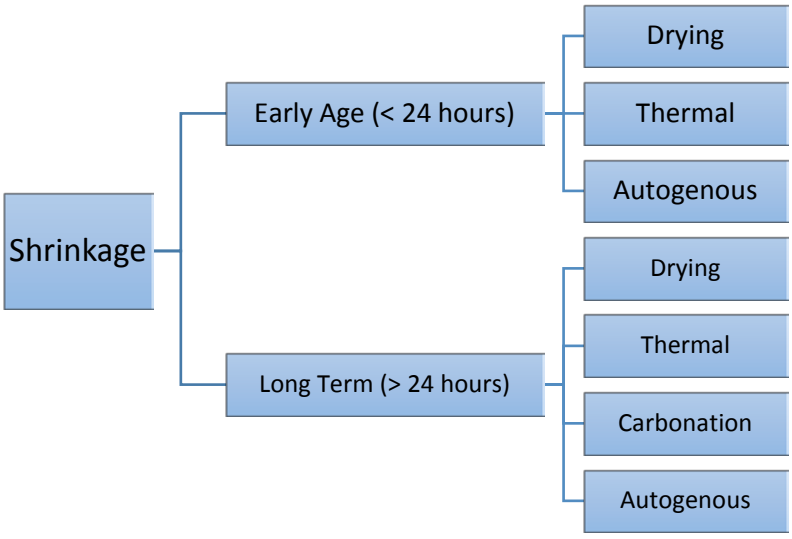

Figure 4.1: The classification of shrinkage of concrete materials [17]

The part of drying shrinkage is the change in volume of specimen when there is losing water from the capillary pores. It causes the tensile stress in the capillary pores to decrease the volume. Scherer illustrated the stages of drying shrinkage by a series of schematically diagram [18]. The initial gel consists of continuous solid network incorporating a continuous liquid phase (Figure 4.2). When evaporation occurs on the solid phase, the liquid tends to spread over it due to the solid/vapor interface has a higher energy than the solid/liquid interface. The tensile stress appears in the liquid and the compressive imposes on the solid network as water moves to cover solid which result in shrinkage (Figure 4.3). While the moisture contained in gel decrease, the radius of the meniscus being developed decrease as well. The decrease of radius of the meniscus will continue until it reaches its minimum value which is the radius of the pore (Figure 4.4).

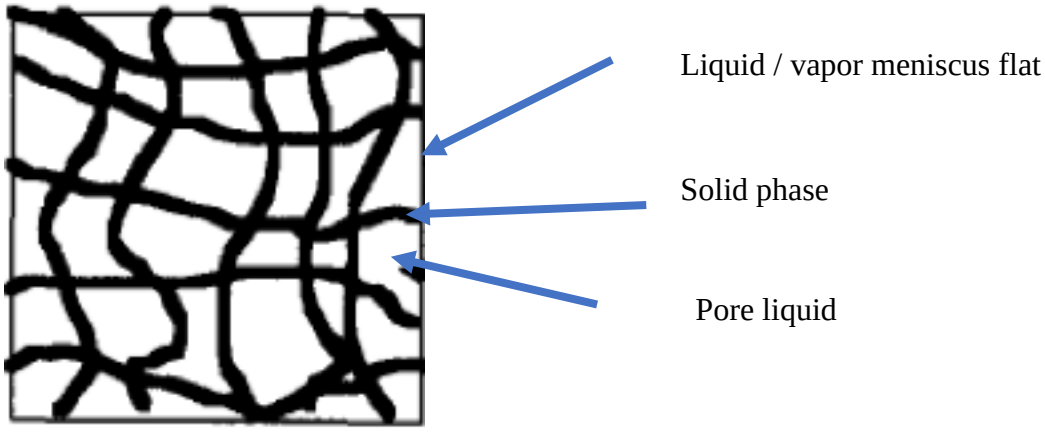

Figure 4.2: Initial stage of shrinkage[18]

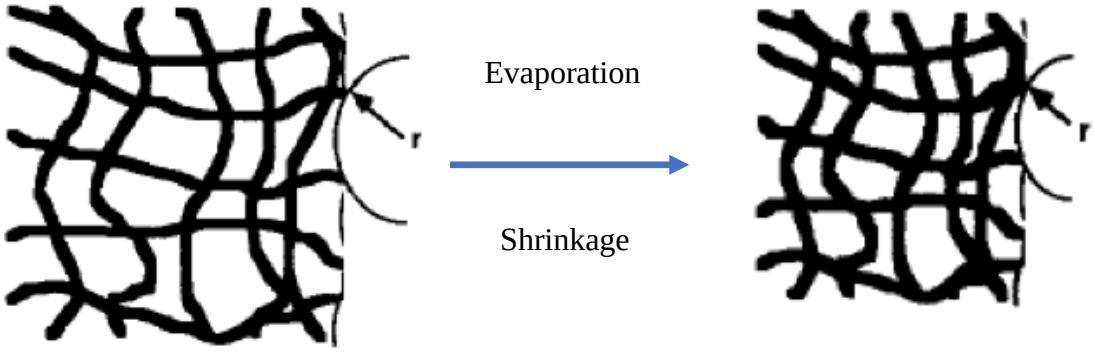

Figure 4.3: Evaporation from surface [18]

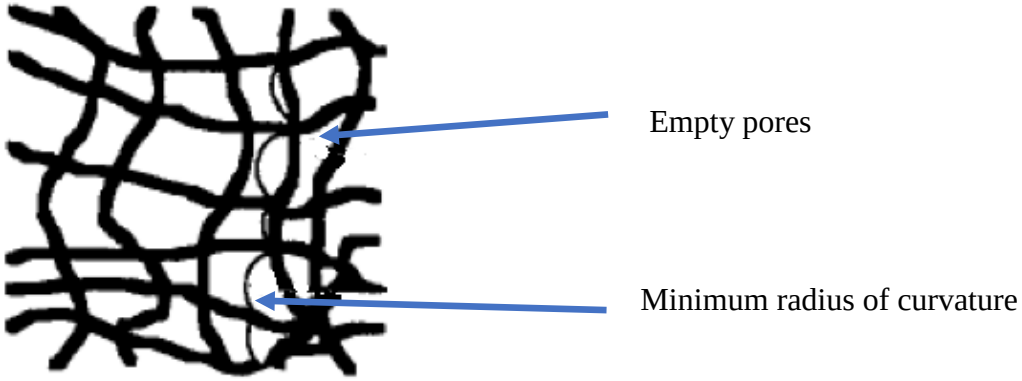

Figure 4.4: Dry region forms [18]

Drying shrinkage is a long term shrinkage behavior that all of the tests were started after 24 hours after casting. Wallah and Rangan used two curing procedures: (I) ambient temperature for 3 days; and (II) heat-cured at 60 ºC for 24 hours and 2 days in water at room temperature. All of the measurements were started after 3 days. The drying shrinkage result of specimens under ambient temperature was about 1500 micro-strains after 3 months which was two to three times higher than an equivalent OPC based concrete. However, heat-cured fly ash-based geopolymer concrete underwent lower shrinkage behavior with only 100 micro-strains after 3 months [19]. Sagoe-Crentsil also did a similar test of fly ash-based geopolymer concrete. The specimens were heat-cured under 60 ºC for only 6 hours and then stored in a fog room under room temperature. The

drying shrinkage result was 250 micro-strains after 3 months [20] which was higher than what Wallah and Rangan obtained. It seems the short heat curing duration gave out the different results. A. Castel et al. started testing drying shrinkage after only one day. Shrinkage strains were about three times higher than OPC concrete. They claimed that even extend the duration of heat curing, it only provided modest benefit in shrinkage [21].

Atis et al. [22] studied the influence of activator on shrinkage of alkali-activate slag mortar. In their experiment, the shrinkage of sodium silicate solution activated slag mortar had a high drying shrinkage about six times more than PC mortar. And sodium hydroxide activated slag mortar has three times shrinkage more than PC mortar. Ranjani [23] studied the shrinkage of fly ash-slag based geopolymer concrete. He used mixture of potassium hydroxide (KOH) and potassium silicate (K_2SiO_3) as an activator and test at different concentration. The results show that drying shrinkage of geopolymer concrete was about three times higher than PC mortar. Besides, while the concentration was higher, drying shrinkage was slightly lower. Lee et al. [24] also claimed that while increasing the amount of slag, shrinkage would increase as well. In addition to geopolymer gel, there was another reaction product of alkali-activated fly ash slag (AFS) paste, C-N-A-S-H gel and there existed other particle such as unhydrated slag and fly ash. Because calcium (Ca) highly existed in slag, the increase of calcium content supplied from the slag contributed to the formation of more amorphous C-N-A-S-H gel. As the result, the matrix was denser that caused higher capillary stress than OPC mortar and it led to higher drying shrinkage. Drying shrinkage performance of fiber geopolymer concrete under different fly ash/ slag ratio will be studied later.

4.2 Experimental Setup

This shrinkage study focused on the drying shrinkage behavior of FGC, where the experimental procedure was according to ASTM C157 [49]. This test method was to determine the length change which measured an increase or decrease material behavior in the linear dimension along the longitudinal axis of unstrained specimens through the laboratory testing. Measurement of length change points out the potential for volumetric expansion of concrete due the various causes. The specimens should be cast in a mold with 625 mm^2 (1 $inch^2$) for cross sectional area and 254 mm (10 inches) for the length. Besides, according the mold design gage studs were cast into the end of each prism specimen. For this test, specimens were exposed to a controlled ambient temperature between 19 to 22 ºC and relative humidity between 40 to 70%.

The initial measurements of length change were started from the next 24 hours after the step of dry heat-curing then keep measuring everyday shown as Figure 4.5. Length change was calculated by the equation (4.1)

$$L = \frac{(Lx - Li)}{G} \times 100, \tag{4.1}$$

where, Lx = comparator reading of specimen at x age minus comparator reading of reference bar at x age. Li = initial comparator reading of specimen minus comparator reading of reference bar at that same time. G = nominal gauge length, 10 inches. The mass change was also measured at the same time under the same conditions as the drying shrinkage test for understanding the loss of water from the capillary pores.

Slag was used to enhance the early strength of geopolymer concrete. However, the amount of Slag mixed into geopolymer is going influence the performance of drying shrinkage. Thus, three different ingredient proportions that used different FA/ Slag ratio, 10/0, 9/1 and 8/2 were mixed to validating different drying shrinkage behavior. The numbers ‘F10’, ‘F9’ and ‘F8’ refer to the different ratio of FA/ Slag: 10/0, 9/1 and 8/2. In addition, the control specimens that included geopolymer concrete which did not include any PVA fibers and mortar were tested as well. In this test, the images from scanning electron microscopy (SEM) were performed to analyze the polished surfaces of each specimen.

Figure 4.5: Drying shrinkage test setup following ASTM C157

4.3 Experimental Results

In this part of study, the drying shrinkage behavior and effects of various mix parameters on FGC specimens were studied. Since mixing Slag into the process of geopolymerization has been found can enhance the early strength of geopolymer concrete, the regular FGC specimens in this studies were always mixed with 8/2 FA/ Slag ratio. However, increasing the amount of Slag in geopolymer concrete caused higher shrinkage behavior than geopolymer which did not include any Slag. Figure 4.6 shows the average drying shrinkage of FGC specimens for three different FA/ Slag ratios, 8/2, 9/1 and 10/0. It can be seen that F10 specimens had the lowest shrinkage behavior which the strain approached to 0.113% at the 28^{th} day. The strain of F9 and F8 specimens approached to 0.116% and 0.119% at the 28^{th} day. Figure 4.7 is the percentage of mass loss for each tested specimen. The mass loss can be considered as moisture loss due to water evaporation. F10 specimens had the highest mass loss of 4.2% at the 28^{th} day. For F9 and F8 specimens were 3.6% and 2.8% at the 28^{th} day.

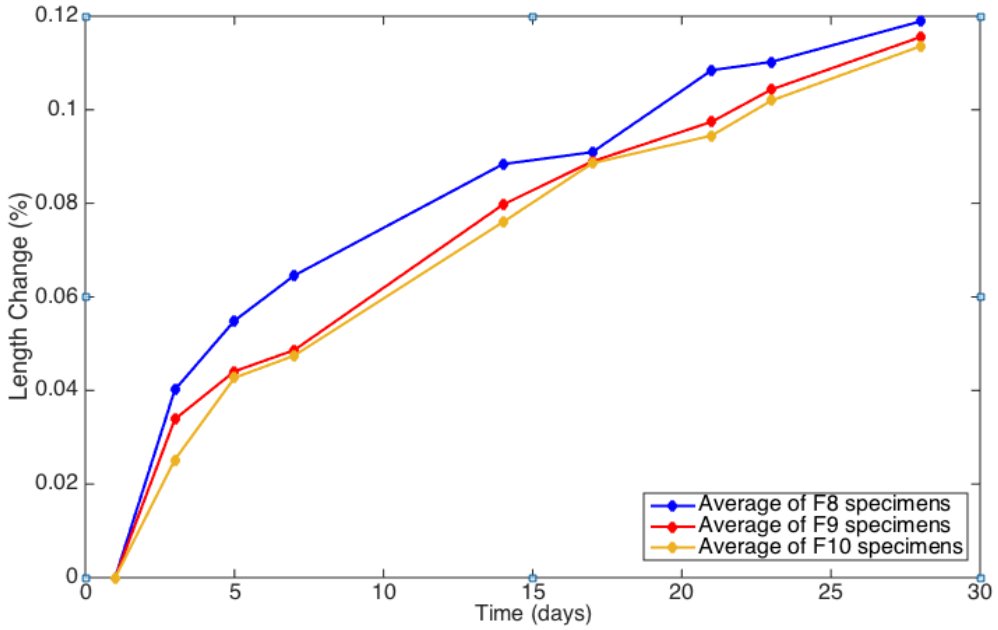

Figure 4.6: Drying shrinkage for FGC with different FA/Slag ratios

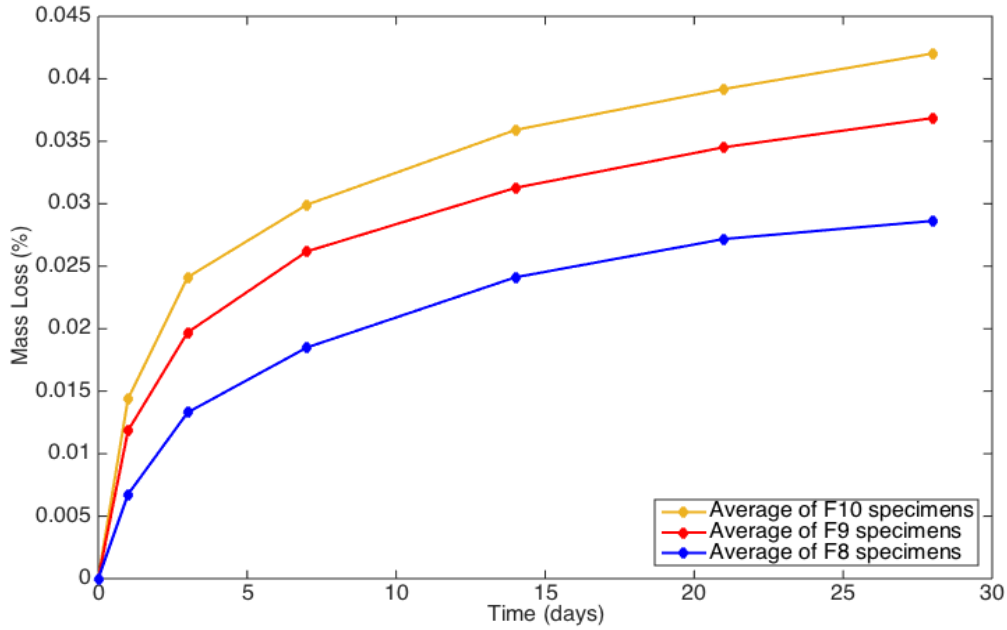

Figure 4.7: Mass loss of FGC specimens with different FA/Slag ratios

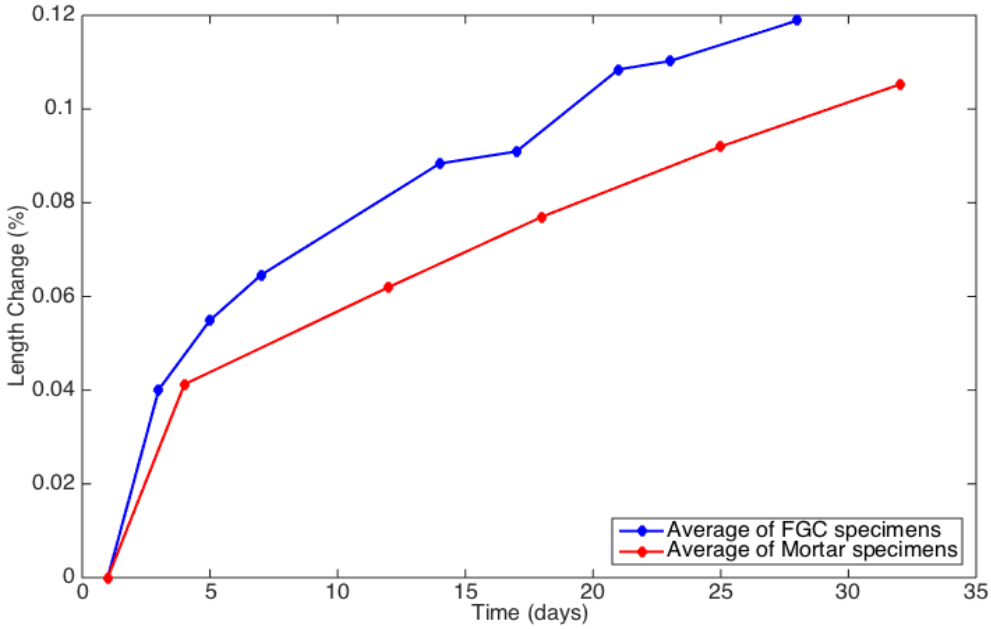

Figure 4.8: Drying shrinkage of FGC compared with control mortar specimens

The drying shrinkage results of comparing FGC specimens and control mortar specimen are shown in Figure 4.8. FGC specimens had slightly higher length change than mortar specimens. In the period of shrinkage measurement, FGC specimens had more than 0.11% length change and mortar specimens had approximately 0.10% length change.

4.4 Discussion

The drying shrinkage behavior of FGC was studied for different mixture proportion. The drying shrinkage measurement was started from the third day after casting and curing. Therefore, in Figure 4.6 & Figure 4.8, the time ‘one’ in the drying shrinkage length change respect to time in days represented the first initial measurement at third day after casting.

Comparing with the interface between solid and vapor and the interface between solid and liquid, the former one has higher energy [53]. As the result, while water moves due to evaporation, it would develop tensile stress and leads to drying shrinkage. In general, this phenomenon occurred more seriously in capillary pore rather than larger pore. The water trapped in these pore is difficult to evaporate from this pore structure; thus, it would generate higher tensile stress and lead to drying shrinkage. In other words, as the density of concrete increases by the formation of more reaction products, the total porosity decreases and the volume of larger pore decreased simultaneously as well. Since more amount of capillary pore presents in the matrix, drying shrinkage behavior become more apparent.

The observations from SEM of specimens with different FA / Slag (F/S) ratio are showed in Figure 32-34. Comparing with these three figures, Figure 4.9 shows the specimen which F/S ratio = 10 had the highest amount of unreacted FA sphere particle (the grey parts) and some larger pores (the black parts). In this F10 specimen, it did not have a dense matrix structure. Figure 4.10 & Figure 4.11 are the specimens that F/S ratio = 9 and 8. It shows that while increasing the content of Slag in the mixture, the matrix become denser. Figure 34 shows that the F8 specimen had fewer pores and more compact structure than F9 and F10 specimens. In addition, it was found that more unreacted Slag particles were observed in the F8 specimen than in F10 and F9 specimen, whereas there was less unreacted FA sphere in the F8 specimen. As the amount of Slag content increased and FA content decreased in the material, more unreacted Slag particles and fewer unreacted FA spheres were observed by SEM. Due to the shrinkage, there were

still some micro-cracks observed on F8 specimen. As the former results, while increasing the amount of Slag content, the shrinkage might increase due to the finer pore structure.

The moisture loss of F8, F9 and F10 are presented in Figure 4.7, and according to Figure 4.9 - Figure 4.11, It showed that while the concrete matrix become denser it would display lower moisture evaporation. As the concrete had looser structure, it has larger pore size. Due to the reason, the moisture was not easily trapped in the pores. Thus, it only needed less energy consumption for water to escape from pore and then produced less tensile stress in the process of evaporation. As the result, the looser concrete structure had higher moisture loss.

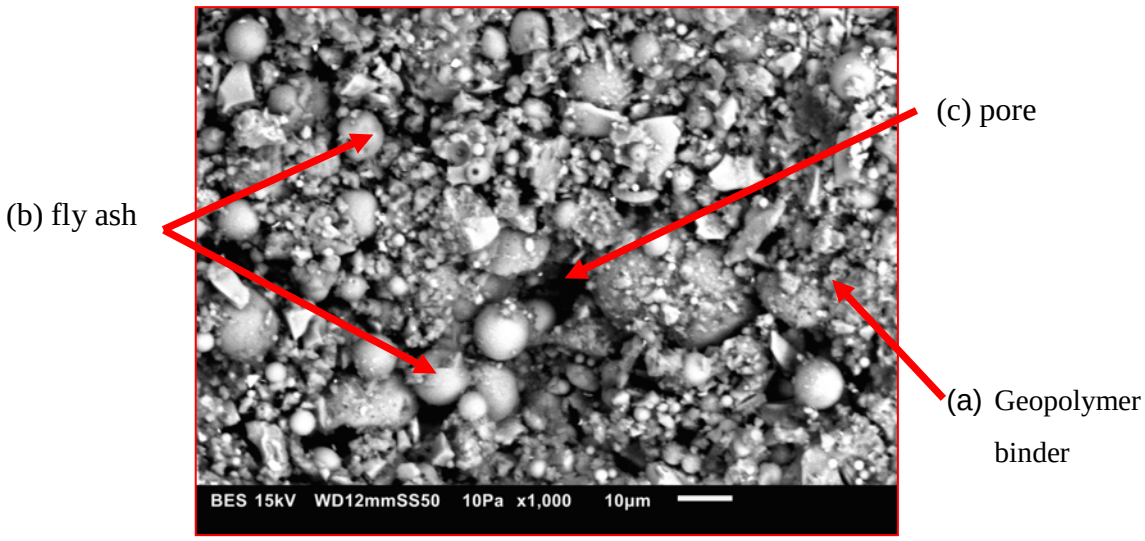

Figure 4.9: SEM image of F10 showing the presence of (a) geopolymer binder, (b) fly ash and (c) pore

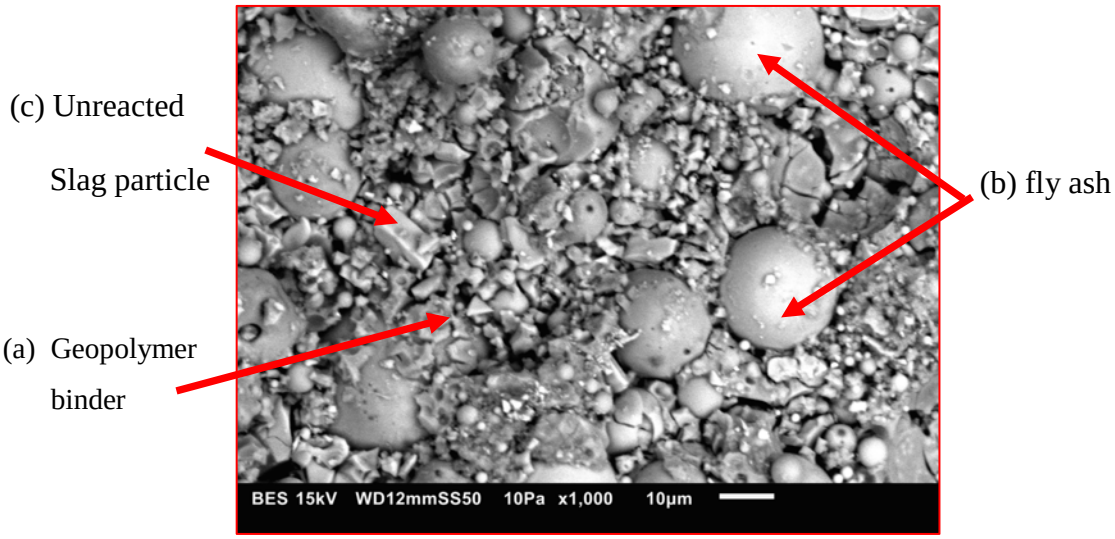

Figure 4.10: SEM image of F9 showing the presence of (a) geopolymer binder, (b) fly ash and (c) unreacted Slag particle

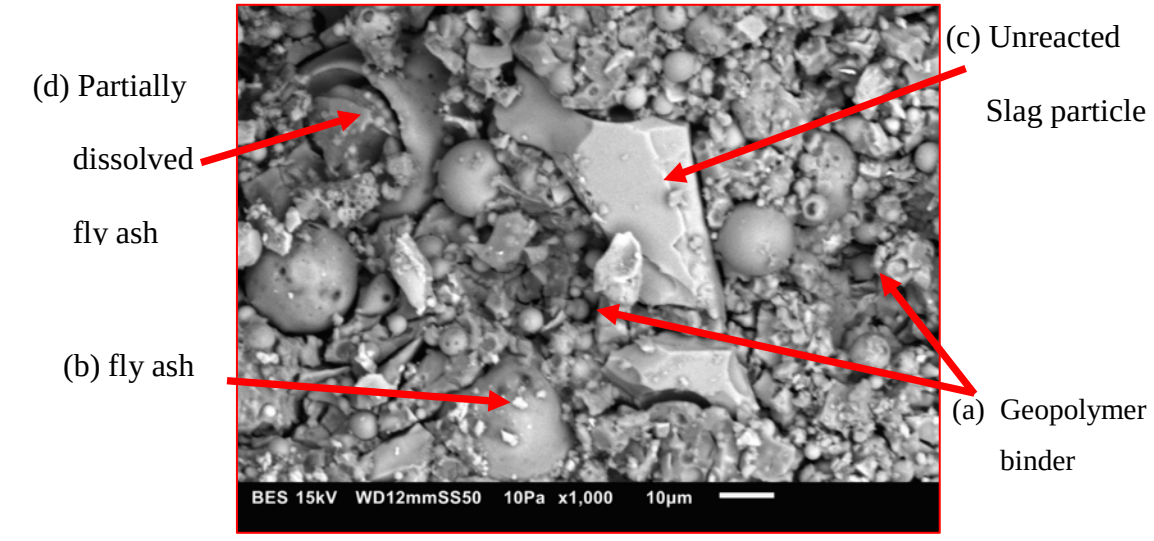

Figure 4.11: SEM image of F8 showing the presence of (a) geopolymer binder, (b) undissolved fly ash, (c) partially dissolved fly ash and (d) unreacted slag particle

CHAPTER 5: ALKALI-SILICA REACTION

5.1 Introduction

Since a number of concrete structures in the U.S.A. were observed to develop severe cracking in 1923, alkali-aggregate reaction (AAR) was recognized as one of a cause of concrete deterioration. AAR is the chemical reaction occurred in concrete that between the silica from aggregates and the hydroxyl (OH^-) ions associated with sodium (Na) and potassium (K) from exterior [25]. AAR contains alkali-silica reaction (ASR) and alkali-carbonate reaction and ASR is a slow reaction that takes 20 to 30 years in temperate and arctic regions to become apparent. Exposing to sever conditions such as freeze, seawater, etc. usually accelerates the process of damage and decay.

ASR usually involves poorly crystallized silica in the aggregate which exposes to the concrete interior at pH 14 and also forms hygroscopic alkali-silica gel [26]. ASR will occur only under the following three conditions [27]: (I) Sufficient fluid. Water plays an essential role of transport medium for alkali-silica gel to absorb and expand. While relative humidity (RH) is in the range of 80 to 90%, it has been reported that is the critical limit for developing ASR [28]. (II) Sufficient alkalis. As shown in Figure 5.1. The pore fluid contains alkali ions such as Na or K can invoke the dissolution of $Ca(OH)_2$, in order to balance the increasing concentration of OH^-. This higher alkali concentration environment increases the dissolution of silica (SiO_2) from the alkali reactive aggregates. Na or K reacts with dissolved silica and turns it into silica gel [29]. (III) Aggregate can be reacted with alkali. The common aggregates usually contain rocks, sands and gravels

that exists different form of silica can react with alkalis. Those poorly crystalline, lattice defects, micro-porous easily occur the reaction [30]. ASR can be prevented by eliminating at least one of the three conditions that described above.

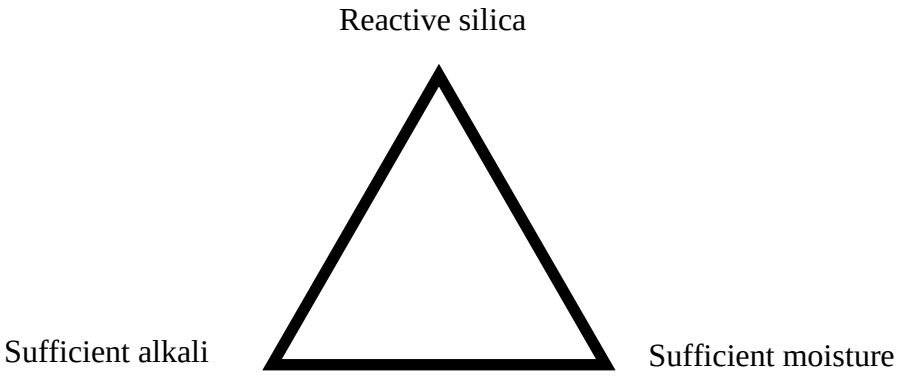

Figure 5.1: The three necessary conditions for ASR to induce damage in concrete [27]

The significant part of chemical reaction mechanism of ASR is silica dissolution in high pH environment. The composite structure of SiO_2 is three-dimensional linked silica tetrahedral with sharing their apical oxygen (O_2-Si-O_2). Nevertheless, the surface of structure has unsatisfied charges which usually appear in poorly crystalline silica. Dissolved OH^- in the solution attaches to those unsatisfied siloxane bonds (Si-O-Si) that is on the silica surface will form silanol (Si-OH) so called Alkali-silica gel. Alkali-silica gel forms according to a two-step reaction. The first part represents an exchange reaction which replaces H^+ in the silanol with Na^+ dissolved in the concrete pore fluid shown as equation (5.1)

$$H_{2x}SiO_{2+x} + 2xNaOH \rightarrow Na_{2x}SiO_{2+x} + 2xH_2O. \quad (5.1)$$

The reaction product is amorphous sodium silica gel and this product cause expansion in concrete structure. In the second part, the over amount of OH^- presents in pore fluid could break down the siloxane bridges of Na-gel and opening up the structure for further water imbibition. This part of reaction exchanges Na in the previous silica gel for dissolution shown as equation (5.2) [31]

$$H_{2x}SiO_{2+x} + 2xNaOH \rightarrow Na_{2x}SiO_{2+x} + 2xH_2O. \quad (5.2)$$

The potential of ASR in geopolymer has been proved that is relative lower than OPC concrete due to the formation as a dense bond in the vicinity of the aggregates after the initial reaction [32]. Since geopolymer concrete is activated by alkali solution, those alkalis involved in the chemical reaction then converted the FA existed in the component into the cementitious binders and zeolite crystals. Owning to the experimental results, the expansion of specimens due to ASR was not detected in these geopolymer-based fly ash mortars. Due to alkali solution in geopolymer played a role of activator, there were some unutilized alkalis attacked the reactive aggregates, initiating ASR when the material was still in the form of gel. However, the ASR product (silica gel) was not found to be expansive. The reason could be the lack of an instigator, readily available calcium. In addition, ASR has been found out that is not only helpful in building a stronger bond at the paste-aggregate interface of geopolymer concrete, but also enhancing the strength of the material.

Kunal et al. claimed that comparing ASR between OPC concrete and geopolymer concrete, OPC concrete exhibited higher average expansion under a 90 days exposure to

1M NaOH solution at 80 ºC. Only a slight expansion of geopolymer concrete presented under the alkali and elevated temperature environment, as the result of re-initiation of the geopolymerization process of unreacted FA particle. It also led to lower porosity and higher strength [33]. Raphaelle et al. studied ASR behavior of metakaolin-based geopolymer concrete. The results showed that though geopolymers contained high concentration of alkalis, were abler to resist ASR than OPC. Besides, there was no characteristic swelling or any significant loss of rigidity was observed on geopolymer specimens. They concluded the reasons in the following phenomena: fast decrease of the pH value, and lack of calcium in the new form products or accommodation of the gels in porous network. They also observed the reaction products covered the entire surface of the glass grains in the sand and decreased the adhesion between sand and geopolymer [34]. Sindhunata et al. found out while increasing the hydroxide concentration of alkali solution led to the collapse of the mesoporous geopolymer gel structure and formation of detectable quantities of crystalline zeolites. The zeolitic products were the same products observed in geopolymer. As the result, the reaction can be considered as some extent continuation of the initial geopolymerization process that built a stronger geopolymer matrix [35]. In this study, the ASR behavior of fiber geopolymer-based concrete will be investigated.

5.2 Experimental Setup

The ASR test of FGC and control mortar specimen was based on ASTM C1260 [50] which can detect the potential for deleterious internal expansion from ASR of aggregate in concrete prisms. This method provides an accelerating ASR process for those

aggregates that react slowly but produce expansion in the late reaction. The specimens were casted in the same prism mold as drying shrinkage test did. For conditioning the specimens, the specimens were stored in the container with sufficient tap water to totally immerse them and maintaining them in the oven at a temperature 80 ºC for 24 hours before the test. After conditioning, initial measurement was recorded as soon as the specimens remove from the container. Then immersed all of the test specimens into sufficient NaOH solution with the concentration 1 M at 80 ºC for another 14 days (Figure 5.2). Recorded the length change every day periodically by the method from ASTM C157 [49] and calculated the strain. It needs be noticed that the time elapse between removal and return of the specimens from water or NaOH solution should not over 10 minutes.

Figure 5.2: ASR specimens immersed in 1 M NaOH solution following ASTM C1260

5.3 Experimental Results

The results of the expansion test were performed as ASTM 1260[50], for each mortar and FGC prism specimens were immersed in 1 M NaOH solution at 80 ºC and the results were summarized in Figure 5.3, red part represented the results of control mortar specimens and blue part represented the results of FGC specimens. Different kinds of sand were mix into each mortar and FGC specimens. For regular mortar specimens, the river sand was selected as an aggregate to fill up the cement paste. On the other hand, well-crystallized quartz sand was used to mix FGC specimens, thus no alkali-silicate reaction was expected on FGC specimens. For control specimens, the volume of mortar bars showed the increasing tendency since they were immersed into the NaOH solution at 80 ºC. However, in the contrast, the volume of FGC specimens not only did not expand in the same condition, but also slightly decreased during the 14 days test. The control mortar showed the average expansion of 0.24% on the 14^{th} day and it kept increasing to 0.29% on the 26^{th} day. FGC specimens had an average shrinkage of 0.036% on the 14^{th} day. Figure 36 also presents the classification which is according to the appendix of ASTM 1260 [50]. The measurement of mortar specimens falls between 0.1 and 0.2 % in the beginning, which can be either harmless or harmful in the field performance. However, after a period of time, the expansion was greater than 0.2% and it was deleterious to the structure. FGC specimens appeared to be better than the mortar in this field of durability as the expansion did not over 0.1% in any of the specimens.

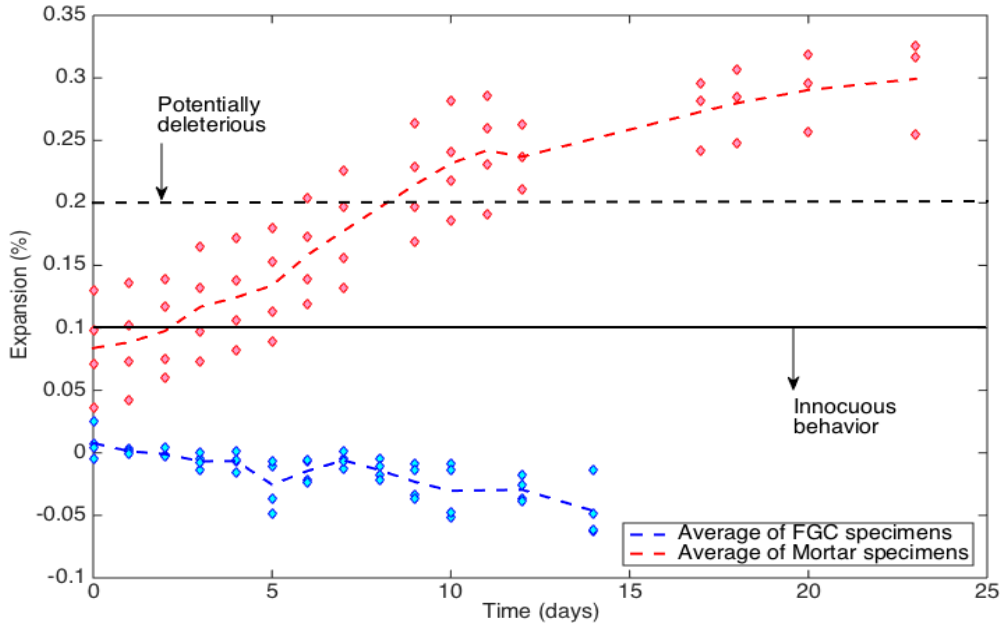

Figure 5.3: Length change of FGC compared with control mortar prism specimens

5.4 Discussion

ASR usually occurs when the following three conditions are satisfied, sufficient fluid, sufficient alkali and aggregate which can be reacted with alkali. In this experiment, sufficient alkaline solution and elevated temperature of 80 ºC were applied to satisfy the external environmental condition. As the result, the aggregate which was mixed into concrete could be tested whether or not it had potential to carry out ASR. A graph of length elongation versus time for FGC and mortar prisms specimens are shown in figure 36. Each data point on the figure represented the average of four values. The mortar specimens were found to be in the deleterious zone that indicating high risk for ASR. In the contrast, FGC specimens were considered to be innocuous. The aggregate of control mortar specimens used regular river sand in the mixing and FGC specimens used well-crystallized quartz sand. Figure 5.4 shows the results of each different sort of sand after

immersing in 1 M NaOH solution. There was alkali-silica gel apparently appeared on the surface of regular river sand after it exposed to high pH value solution. On the other hand, well-crystallized quartz sand was not observed obviously change after the test. It can explain that selecting well-crystallized quartz sand as the aggregate for the ingredient of FGC can prevent ASR effect.

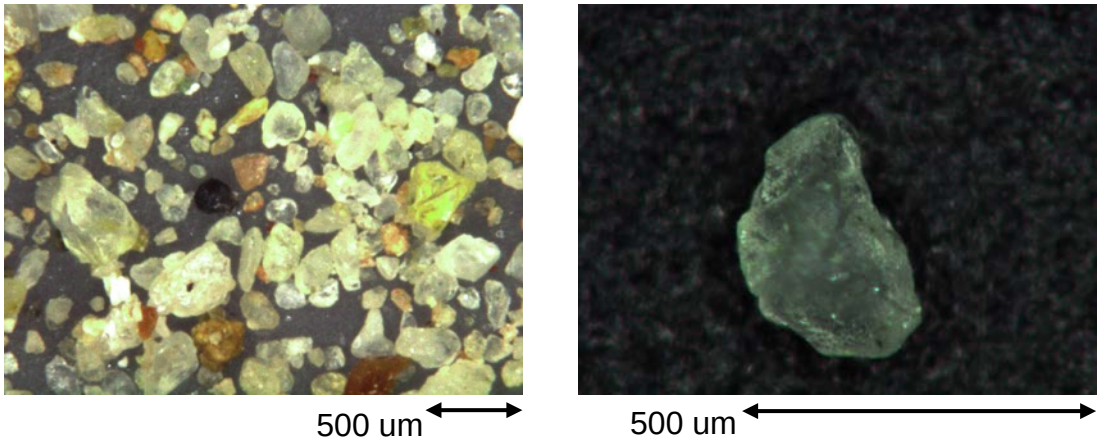

a. Regular river sand before immersing in 1M NaOH solution

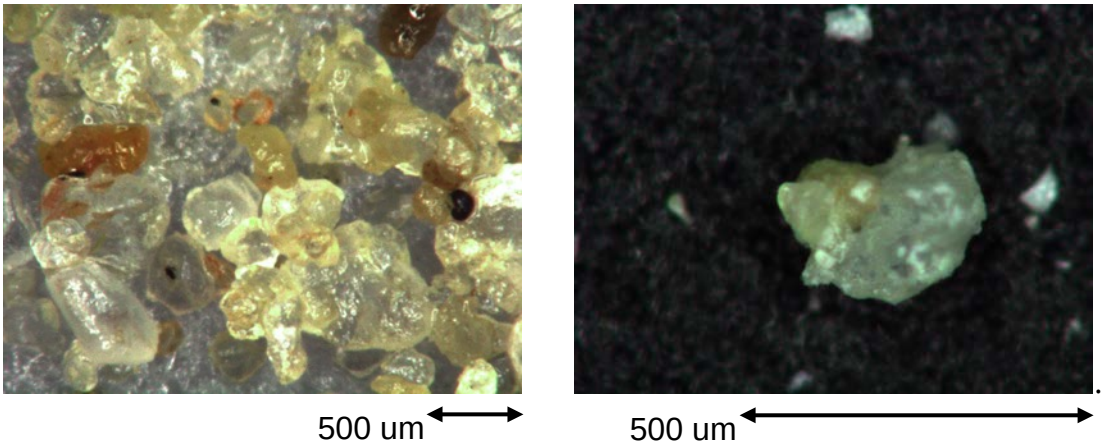

b. Regular river sand after immersing in 1M NaOH solution

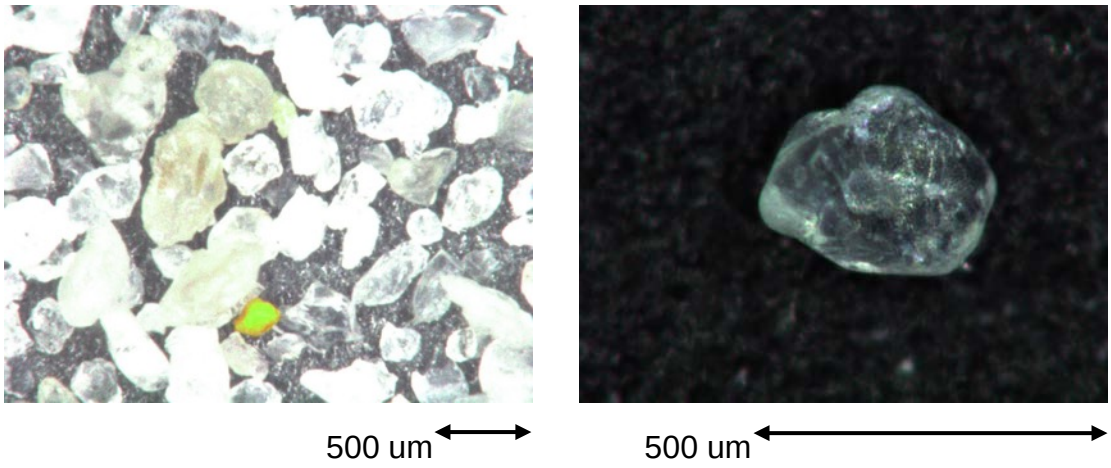

c. Well-crystallized quartz sand before immersing in 1M NaOH solution

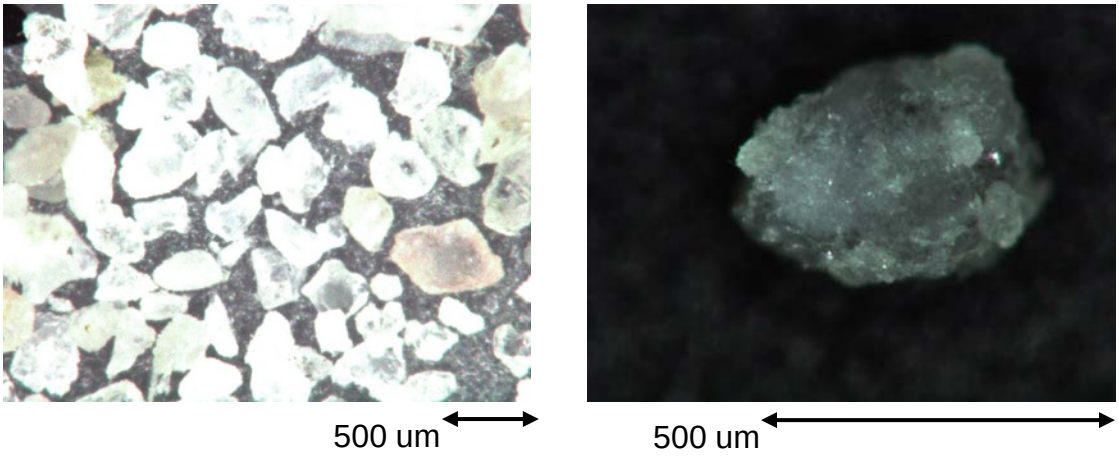

d. Well-crystallized quartz sand after immersing in 1M NaOH solution

Figure 5.4: Microscopy of sand (regular river sand vs. well-crystallized quartz sand) before and after immersion in 1M NaOH solution

CHAPTER 6: WATER PERMEABILITY OF DUCTILE GEOPOLYMER

6.1 Introduction

In order to predict service life for construction material, assessing durability test of water permeability performance is quite important. Water can be considered as a media for transportation that can carry ions that might damage concrete structure such as Cl^-, SO_4^- or CO_2 to penetrate into concrete material and interact with the reaction products or reach the interface of steel. As the result, the understanding of water transport and its correlation with microstructure parameters is a vital step.

The top most significant parameter that influence the water and ion transport can be related to the materials' pore structure, particularly the pore volume, pore size distribution connectivity, and the pore shape [36]. Many studies were done by focusing on various relevant parameters of water permeability of OPC-based concrete [37,38]. However, there is still lack of investigations regard to geopolymer-based concrete.

Y. Ma et al. found out that comparing water permeability with OPC paste, alkali activated fly ash (AAF) was higher than OPC paste for equal reaction age. However, longer curing time at elevated temperature can decrease the water permeability of AAF paste. Although unlike OPC paste, AAF had uniform alumino-silicate gel distributed in the paste and some large cavities rather than large capillary pores were observed, by increasing concentration of alkali and silica can lower the porosity and finer the pore system [39]. In this study, the performance of water permeability of geopolymer-based concrete and fiber geopolymer-based concrete will be discussed.

6.2 Experimental Setup

In this part of experiment, the concrete specimens were casted into a beam shape with 10.16 x 10.16 x 40.64 cm (4 x 4 x 16 inches) and demolded 24 hours later after casting then dry heat-curing the specimens for another 24 hours (Figure 6.1). The Germann water permeability test (GWT) was adopted to measure the flow of water on a designated surface during a period of time under a defined pressure. First, in order to installed anchors and pliers to fix the attaching water chamber, two holes that 8 mm for diameter and 5 cm for depth with an internal distance of 25 cm were drilled on the specimen surface. The water chamber was firmly attached to selected surface through a 15 mm gasket and fixed with two pliers that were anchored into the specimen (Figure 6.2). Filled water into the water chamber and applied defined pressure into concrete specimen surface. The pressure decreased while water started permeating into concrete specimen and record the micrometer gauge reading over 5 minutes. The difference in gauge reading from the start of test and after time period was the index for the water penetration. Calculation of the depth of water penetration can be done by the following equation (6.1)

$$h_t = \left(\frac{d}{D}\right)^2 (g_0 - g_t), \tag{6.1}$$

where, h_t = water penetration depth at time t (mm), d = diameter of steel pin (10 mm), D = inside diameter of water chamber gasket (62 mm), g_0 = micrometer gauge reading at the beginning of measurement (mm), g_t = micrometer gauge reading at time t (mm).

In addition, to determine the coefficient of water permeability of concrete specimens, flux needs to be calculated at the first place. The flux can be calculated for a given water pressure by the equation (6.2)

$$q = \frac{B \times (g1 - g2)}{A \times t}, \tag{6.2}$$

where, B = the area of micrometer pin being pressed into the chamber, 78.6 mm^2 for the 10 mm pin diameter. , g1 and g2 = the micrometer gauge reading in mm at the start of the test and after the test has been finished, A = the water pressure surface area, 3018 mm^2 (gasket inner diameter 62 mm), t = the time which the test is performed over in seconds.

The measured flow rates were then used to calculate the coefficient of water permeability by using Darcy's equation (6.3)

$$C = \frac{q}{P/L} \ (mm^2 / sec \bullet Bar), \tag{6.3}$$

where, Q = flux (mm/s), P = the pressure selected (BAR), L = the length the pressure is applied over, 15 mm (the width of the pressure gasket).

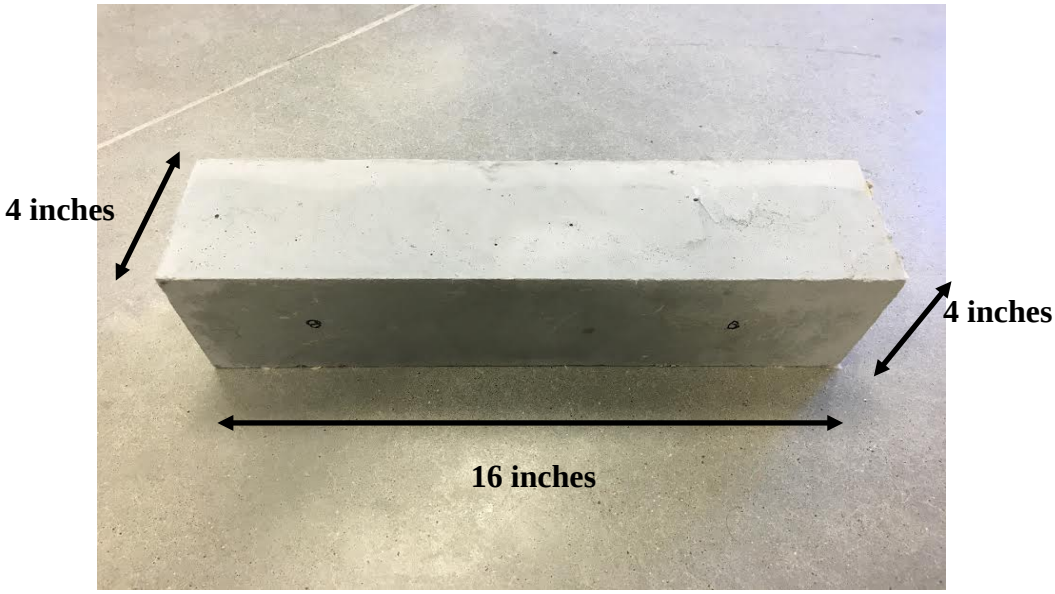

Figure 6.1: Beam specimen for water permeability test

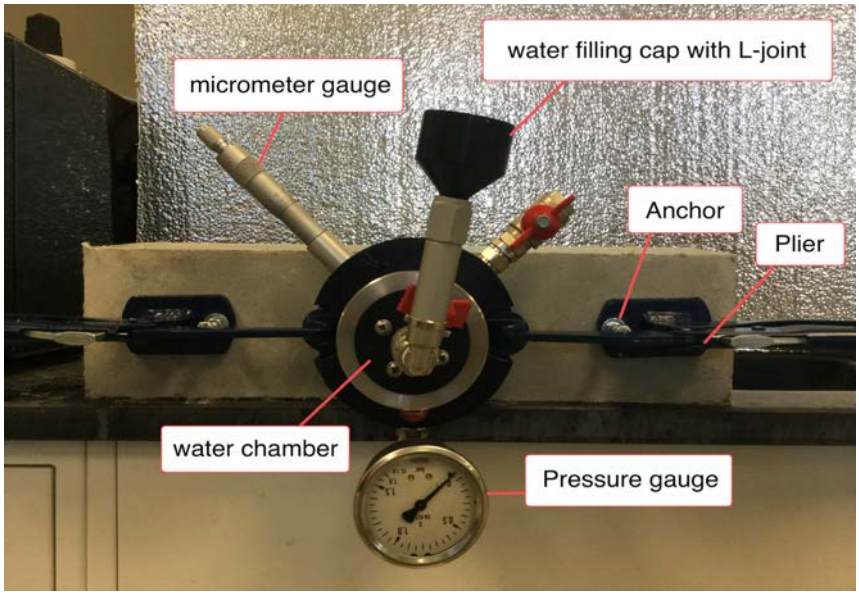

Figure 6.2: Water permeability test setup

6.3 Experimental Results

Figure 6.3 & Figure 6.4 present the results of the depth of water penetrating into the specimen respect to time. The measurement points were calculated by equation 5. The

depth of water penetration has been found that was a linear function of the square root of time. The following equation (6.4) can be fitted to the data.

$$h(t) = a + s\sqrt{t}\,, \tag{6.4}$$

where, a is the intercept and s is called the sorptivity index which is in units of $mm/t^{0.5}$. The Sorptivity index can express the water migration rate in the microstructure of the material. Lower Sorptivity index value represented a higher durability for water permeability. In this test, FGC specimen showed poorer resistance of water permeability. The micrometer gauge (20 mm) was reached to the maximum limit at 135 seconds under 0.25 bar water pressure on the FGC specimens. However, on the regular cement-based concrete specimen, it took almost 200 seconds for micrometer gauge to reach the maximum limit under 0.25 bar water pressure condition. The sorptivity index of FGC was found to be $0.0606\ mm/\sqrt{s}$ and control concrete was found to be $0.04969 mm/\sqrt{s}$. Using equation 6 and 7 can also calculate the water permeability coefficient by Darcy's law. The water permeability coefficient of FGC specimen was 0.264 mm/sec^2-BAR and control concrete specimen was 0.194 mm/sec^2-BAR. Both of the result of the sorptivity index and water permeability coefficient pointed out that FGC specimen had lower water permeability resistance than regular concrete specimen.

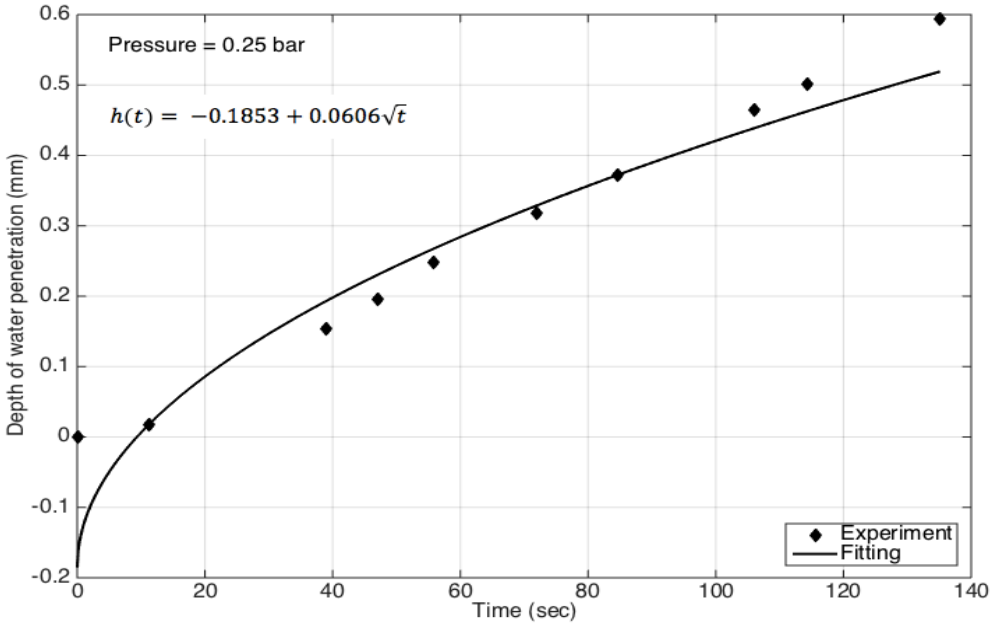

Figure 6.3: Depth of water penetration of FGC specimen

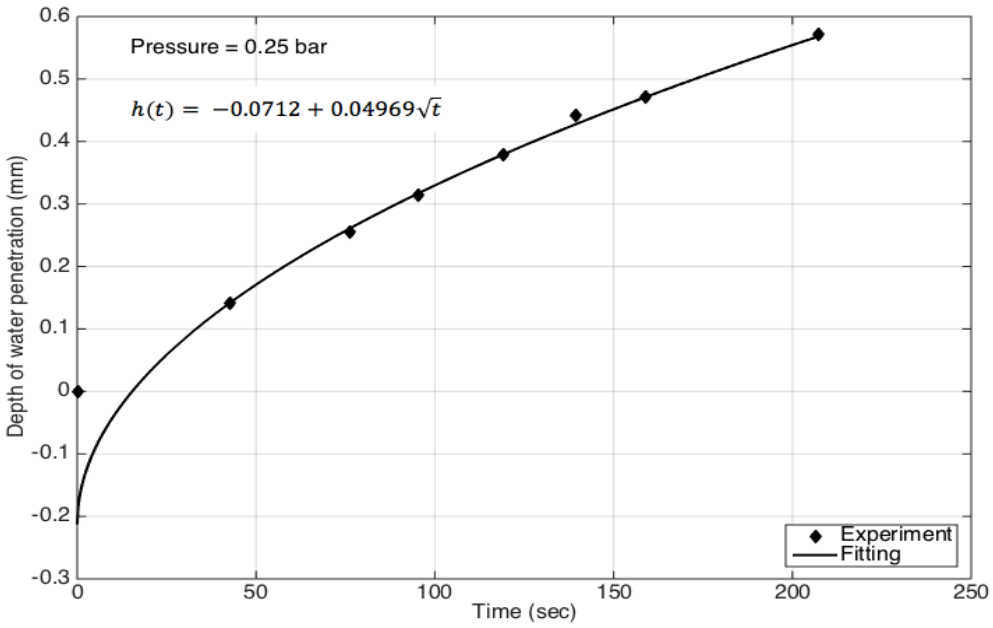

Figure 6.4: Depth of water penetration of control mortar specimen

6.4 Discussion

The pore structure development of concrete specimen is the main reason to effect the water permeability of concrete. Both of FGC and regular mortar material, the pore size decreased to a lower diameter with an increased curing age. For regular mortar material, the reaction process of hydration continuously took place for a long period, up to 28 days or above. The volume of the capillary pores kept decreased until the reaction products totally plugged into those pores. Similar to C-H-S gel is the main reaction product presented in mortar, the main product of geopolymer is alumino-silicate gel. However, the volume of alumino-silicate gel was reported to be lower than C-S-H gel in mortar. The amount of alumino-silicate gel was not enough to block the pores, thus, the pore size was not decrease effectively along the age [39]. The possible factor that cause this difference might due to the most part of the reaction in geopolymer matrix was completed within approximately 7 days. Therefore, there was no sufficient reaction products formed to fill in the pores. As the result, the development of the pore structure of FGC material with time was significant slower than that of mortar material. Thus, it led to high water permeability behavior on FGC material.

CHAPTER 7: CORROSION RESISTANCE OF DUCTILE GEOPOLYMER

7.1 Introduction

Corrosion is a major cause affecting the early deterioration of reinforcing concrete structures. In order to against corrosion, reinforcing steel bars embedded in concrete are usually used high alkalinity of pore water to passivate the presence oxygen. However, while the chloride ions attack the surface of reinforcing steel bars or the pH value of the concrete cover drops down below critical level due to carbonation; the reinforcing steel bars are depassivated. The initial corrosion causes volumetric expansion of reinforcing steel bars to against the concrete cover. The expansion induces tensile stress and leads longitudinal cracks occurred in the concrete paste along the corroding reinforcing bar. Therefore, the degree of corrosion could be considered as one of the main parameters to predict the service life of concrete structure.

There are two ways of methodologies to protect reinforcing steel bars from corrosion. The first method of protection is approaching by delaying the initiation of corrosion. The second one includes that extending the active corrosion period and the period between corrosion initiation and the end of service life. Morris et al. studied various metals embedded in fly ash geopolymer-based mortar. They demonstrated that as long as the geopolymer matrix was alkaline, the passive film around the reinforcing steel bar could be maintained [40]. Miranda et al. claimed that activated fly ash mortar had same effective behavior of passive steel bars as OPC concrete in chloride free environment. Besides, the total porosity was lower for activated fly ash mortar that gave this material a

greater impermeability to retard the penetration of chlorides and atmospheric CO_2. As the result, it could be the reason for passivation effect on the steel bars [41]. Bastidas et al. found out the chloride depassivated the steel bar embedded in activated fly ash mortar was as fast as OPC concrete. And the concentration of the activator affects the resulting pH value in the activated fly ash mortar matrix [42]. Chindaprasirt et al. discussed the the effect of NaOH concentration on chloride penetration by immersing specimens in the marine environment for 3 years. The result showed that increasing the concentration of NaOH can decrease the the chloride penetration and corrosion of embedded steel. In addition, increasing the NaOH concentration in geopolymer can also decrease the percentage of chloride binding capacity as comparing to the total chloride content [43].

In order to investigate the reinforcing steel bar embedded in concrete cover, researchers designed the current experiments. By charging the reinforcing steel bars with impressed voltage and immersing specimens into a sodium chloride solution which was used as an electrolyte that can accelerate corrosion occur in the reinforcing concrete structure. In Yodmunee & Yodsujai's test, they used impressed voltage to accelerate the corrosion on fly ash geopolymer concrete. Geopolymer concrete has little corrosion activity than OPC concrete [44]. M. Olivia et al. studied the corrosion performance of embedded steel bar in fly ash geopolymer by impressed voltage method. They claimed that magnitude of the voltage is only effective way to induce corrosion at different rate. The geopolymer concrete displayed lower current value and higher electrical resistance than control specimen. The results could be contributed to the existing alkalinity in the matrix pore solution. Besides, small cracks on the surface of fly ash geopolymer led no significant increase on the current. By visual inspection can detect that there was high

chloride penetration into the geopolymer concrete but no sever damage on steel bar. As the result, fly ash geopolymer yielded longer time to failure than OPC concrete due to corrosion [45].

Polypropylene fibers have been proved to improve some concrete properties. Whether or not that mixing polypropylene fibers into concrete specimen can reduce corrosion of reinforcing steel bars is interested. Abdul-Hamid et al. added polypropylene fibers into concrete mixture in order to enhance the properties of hardened concretes. The results turned out the polypropylene fibers reinforcing concrete showed no difference with regular reinforcing concrete. In addition, the electrical resistivity of concrete was not significant affected by adding polypropylene fibers [46]. Sahmaran et al. studied the corrosion resistance of engineered cementitious composite (ECC) concrete. Due to the longitudinal crack opening caused by steel expansion from corrosion, chlorides ions can easily attack steel surface and led more sever corrosion. However, the contribution of polypropylene fibers gave high tensile strain capacity and micro-cracking behaviors of ECC that could significantly prolonged the corrosion propagation period and showed lower weight loss of the steel bar embedded in ECC than mortar under same time of accelerated corrosion [47]. Corrosion behavior has already been investigated by lots of researchers, but there still lack of understanding of fiber geopolymer based concrete. In this studied, the corrosion behavior will be discussed by electrical method.

7.2 Experimental Setup

This experimental setup was referred by Florida Department of Transportation (DOT) [51] for accelerate corrosion test and similar accelerated corrosion setup was also used by

other researchers [44, 47, 52]. FGC and other control specimens were casted into cylinder molds with 7.62 cm (3 inches) for diameter and 15.24 cm (6 inches) for height. Embedded a #4 (0.512 inches) steel rebar through the center of the specimen and suspended at 3.175 cm (1.25 inches) height from the bottom of cylinder (Figure 7.1). The FGC specimens were demolded and heat-cured for 24 hours before testing.

The corrosion resistances of each specimen were measured using an accelerated corrosion cell shown as Figure 7.2 & Figure 7.3. In this cell, specimens were partially immersed into 5% sodium chloride (NaCl) solution up to half height, in order to simulate the concentration of seawater in the natural environment. The exposed part of steel bar was connected to the positive terminal of a constant 30 Voltage D.C. power supply and the negative terminal was connected to s stainless steel plate. While the current flow was under continuously logged, the specimens were visually inspected daily for cracks. The crack in concrete can be regarded as an electrical path connecting steel bar and solution. The result would increase current flow dramatically and have visually crack on the surface of concrete specimen. Based on the recorded current, the theoretical resistance can be determined by Ohm's Law (equation (7.1)):

$$R = \frac{V}{I}, \tag{7.1}$$

where, R = theoretical electrical resistance, V = the constant voltage, 30 V, I = the recorded current.

After inducing different degrees of accelerated corrosion exposure, the specimens were broken to retrieve the entire reinforcing steel rebar for the purpose to measure the

mass loss of each reinforcing steel rebar by equation (7.2)

$$\text{corrosion mass loss} = \frac{\text{initial mass} - \text{final mass}}{\text{initial mass}} \times 100\,. \qquad (7.2)$$

The bars for each specimen was cleaned with de-ion water and scrubbed by metal brush to ensure the bars were free from any attached corrosion products.

Figure 7.1: Specimens for accelerate corrosion test

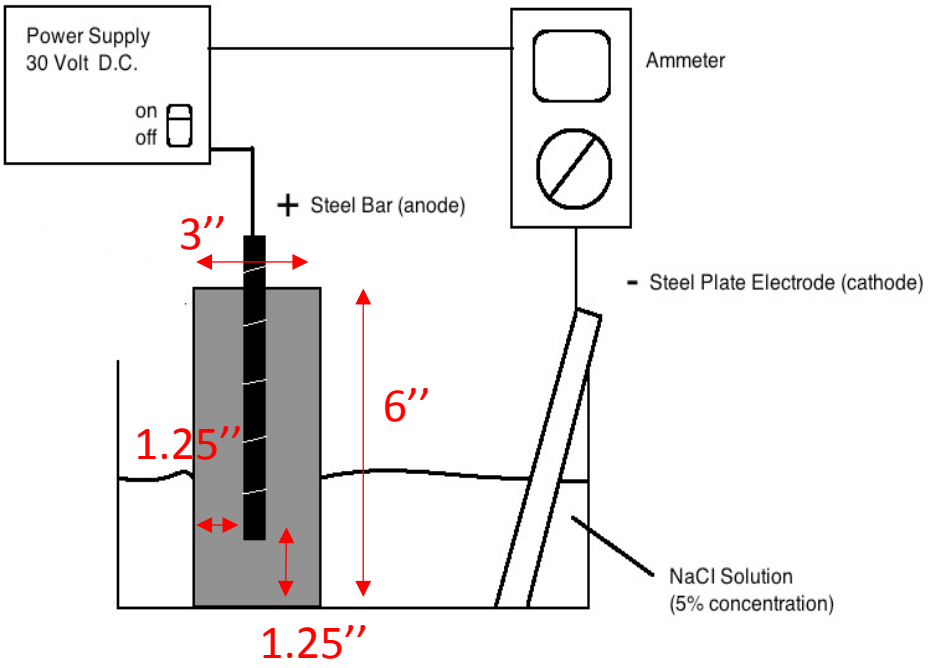

Figure 7.2: Illustration of accelerate corrosion test setup

Figure 7.3: Experimental setup for accelerate corrosion test

7.3 Experimental Results

The current measured during the process of accelerating corrosion test responded as a function of time under a fixed voltage, 30 V that shown in Figure 7.4. The current-time curves were used to determine when the initiation of reinforcement corrosion occurred by observing the instantaneous rise in the curve. It can be seen that in Figure 7.4, the initial current of FGC specimen and control mortar specimens were 0.0097 A and 0.23 A. Due to equation (7.1), the theoretical resistance can be calculated. FGC specimens had higher resistance 3093 Ω than mortar specimen 130 Ω. Since the corrosion product (Fe_2O_3) of reinforcing steel had higher electrical resistance than it used to be (Fe), the part of current drop can be considered as the embedded reinforcing steel started corroded since the resistance of reinforcing steel increased during the process. The corrosion would expand the reinforcing steel and the produced tensile stress caused longitudinal crack on the concrete surface. The instantaneous rose in the curve was owning to the longitudinal crack suddenly occurred. The crack opening was like to enlarge an electrical path for the current that pointed out the reason why the value increased sharply.

For control mortar specimens the current dropped down to 0.13 A after 30 hours. The visually longitudinal crack occurred at this time and the current value dramatically rose up and kept increasing. In the end of the acceleration process, the longitudinal crack with the observation of a 2.5 mm (0.098 inches) size crack width on the mortar specimens shown in Figure 7.5. In the contrast, the current of FGC specimens was smoothly and only presented a little dropped during the test. It decreased from 0.0097 A to 0.0065 A after 120 hours and slightly increase to 0.02 A after 220 hours. Besides, there was no localized large crack observed on the surface of FGC specimens. Instead, a distribution of micro-cracks was observed shown in Figure 7.6.

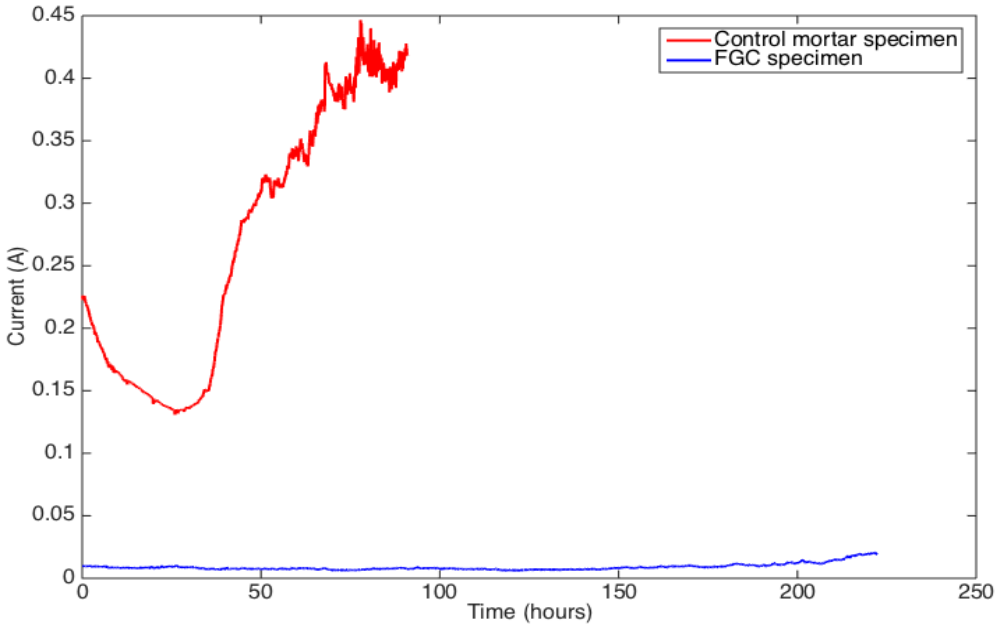

Figure 7.4: Measured corrosion current with time for FGC and control mortar specimens

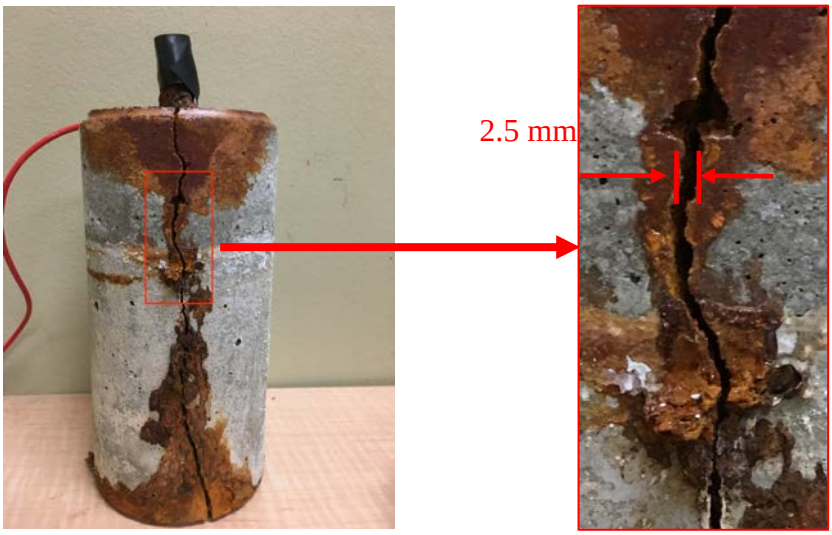

Figure 7.5: Longitudinal crack on control mortar specimen after 92 hours

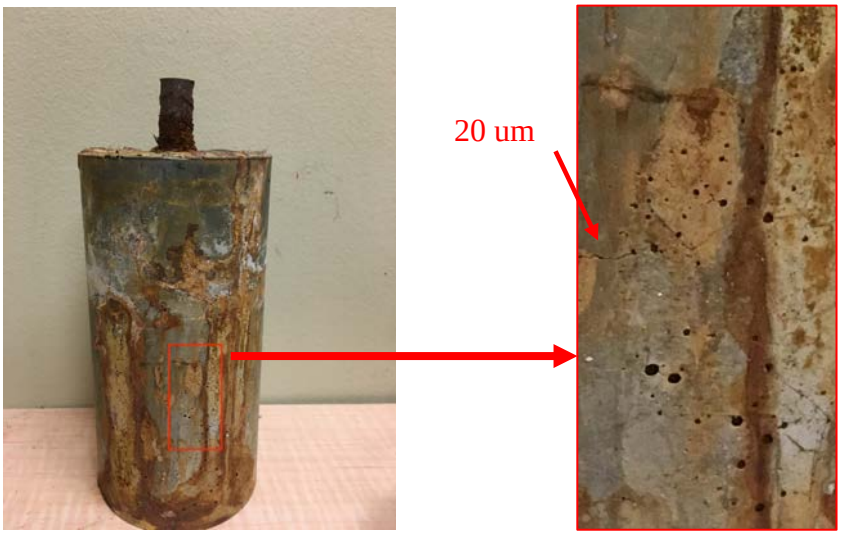

Figure 7.6: Distributed fine micro-cracks on FGC specimen after 222 hours

The percentage of steel mass losses of the FGC and mortar specimens at different accelerated corrosion exposures is showed in Figure 7.7. The average percentage of mass losses of reinforcing steel embedded in FGC specimens were 0.12%, 0.44% and 1.22% at the end of 72, 144 and 222 hours of accelerated corrosion exposure, respectively. In the contrast, regular mortar had much higher mass loss during test. The average percentage of mass losses of reinforcing steel embedded in mortar specimens were 3.1% and 8.4% at the end of 72 and 92 hours of accelerated corrosion exposure, respectively. Figure 7.8 presents the corroded reinforcing steels which were taken out from the tested specimens. The corrosion degree of bars that was took out from mortar specimens can be distinguished by visual observation. In the contrast, the bars form FGC specimens only had slight corrosion that cannot be distinguished by visual observation.

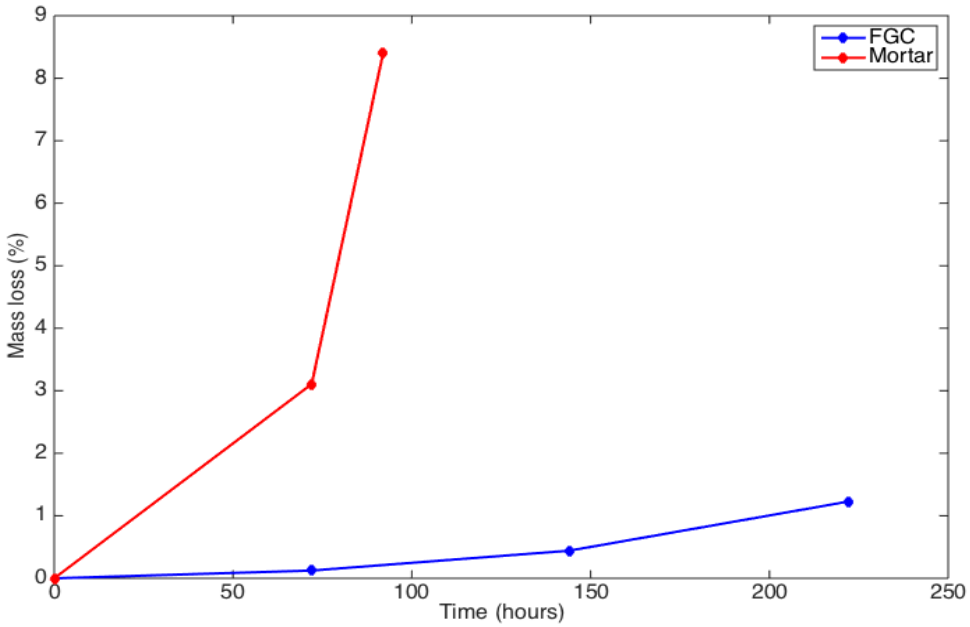

Figure 7.7: Mass loss vs. corrosion exposure time for the steel reinforcement within FGC and mortar specimens

After 222 hours exposure

After 144 hours exposure

72 hours exposure

a. Reinforcing steel bar took out from FGC specimen

After 92 hours exposure

After 72 hours exposure

b. Reinforcing steel bar took out from control mortar specimen
Figure 7.8: Corrosion of reinforcing steel bar

7.4 Discussion

Generally speaking, each of the curves of current and corrosion rate presents in figure 45 can be considered to be inversely proportional to the electrical resistivity of the material [54]. The concrete resistivity is the ability for concrete to obstruct current pass through its structure. The higher electrical resistivity described higher difficulty for ions to travel through the concrete, therefore the concrete inhibiting corrosion. For FGC specimens, high-volume of FA was activated by alkaline solution to result in a denser matrix. Tiny pore size in FGC might explain the observation of higher electrical resistivity. As the result, the higher electrical resistivity of FGC was expected to be associated with longer corrosion initiation.

In general, chloride concentrations increase with increasing crack widths, especially in the deeper depth from the top of the specimens. Therefore, the large cracks can reduce the service life of reinforced concrete structure while during the accelerating initiation of corrosion test; especially the crack width is larger than 0.006 inches [55]. Distribution of micro-cracks instead of large longitudinal crack appeared on the surface of FGC specimen. This tight crack width of the surrounding FGC specimen did not allow

moisture and chloride ions easily accessed to the surface of embedded reinforcement, thus it led to higher corrosion resistance than regular mortar. The micro-cracks tended to be easier plugging by corrosion products than large crack occurred on regular mortar specimen. Once these micro-cracks sealed by corrosion products, the corrosion propagation period would be extended. This behavior of micro-cracks was plugging by corrosion products can be considered as a self-healing performance [55]. These micro-cracks might attribute to the steady state current that was observed even in a long term period of accelerating corrosion test.

According to ASTM G1[56], the corrosion rate based on steel mass loss can be calculated from the following equation (7.3)

$$\text{Corrosion rate} = (\mathrm{K} \times \mathrm{W})/(\mathrm{A} \times \mathrm{T} \times \mathrm{D}), \tag{7.3}$$

where, K = constant (8.76 x 10^7 μm/year), T = time of exposure (hours), A = area (cm^2), W = mass loss (grams) and D = density (7.82 g/cm^3 for steel, from Appendix X1 ASTM G1). The original mass loss for specimens exposed in the accelerated corrosion test was computed by equation (7.2). In addition, the amount of corrosion is related to the electrical energy consumed, thus the theoretical mass loss was estimated by equation (7.4) based on Faraday's Law [57, 58],

$$\Delta \mathrm{W} = (\mathrm{AIt})/\mathrm{ZF}, \tag{7.4}$$

where, A = atomic weight of iron (56 grams), I = corrosion current (amp), t = time elapsed (seconds), Z = the valence of the reacting electrode (2 for iron, $\mathrm{Fe} \rightarrow \mathrm{Fe}^{2+} + \mathrm{e}^{2-}$)

and F = Faraday's constant (96,500 amp-sec). It should be noticed that the corrosion rates are not necessarily constant with time of exposure.

Figure 7.9 compares the mass loss between actual measurement and theoretical computation. There are some possible factors might cause the different value between the actual mass loss and theoretical mass loss. (i) Composition of reinforcement. It is assumed that reinforcement is made of pure iron. (ii) Faraday's law is based on original cross-section. As the cross-section diminished would accompany with error. (iii) The actual mass loss was less than the theoretical mass loss at the first place (at 72 hours accelerating corrosion) due to the protection provided by concrete cover. (iiii) Since the specimens were disconnected from the impressed current for data logging every couple days, natural corrosion might occur at this time to influence the process of accelerated corrosion test. This might lead to higher actual mass loss while comparing with theoretical mass loss in the late experimental measurement. The error becomes larger with a longer accelerated corrosion period.

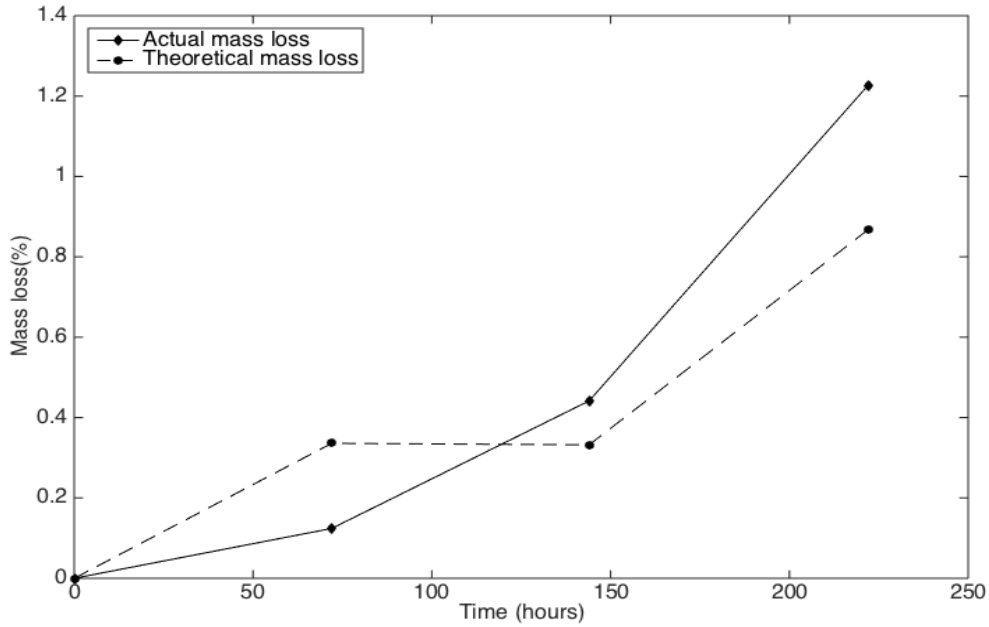

Figure 7.9: Actual mass loss and theoretical mass loss for the steel reinforcement within FGC specimen during accelerated corrosion test

Table 7.1 presents the actual corrosion rate and theoretical corrosion rate that computed by ASTM G1and Faraday's Law [56, 57, 58]. During the process of accelerating corrosion test, the corrosion rate was different at different time measurement. Both of the results between actual corrosion rate and theoretical corrosion rate pointed out those FGC specimens had lower corrosion rate than regular mortar specimens while under same electronic potential. After the crack propagated on mortar specimen, the corrosion rate of mortar grew up rapidly. In the contrast, due to the strain-hardening behavior to avoid large crack appeared on the surface, the corrosion rate of FGC specimens did not have extremely variation like mortar did during the process. In this durability of corrosion resistance test, FGC material had a greater protection to the embedded reinforcing steel than regular mortar material had.

Table 7.1: Actual corrosion rate vs. theoretical corrosion rate

	Time (hours)	72	92	144	222
FGC	Actual rate (mm/yr)	24.50	-	42.88	79.46
	Theoretical rate (mm/yr)	66.34	-	32.25	56.18
Mortar	Actual rate (mm/yr)	612.53	1205.47	-	-
	Theoretical rate (mm/yr)	3647.64	3095.75	-	-

CHAPTER 8: CONCLUSIONS AND FUTURE WORK

8.1 Conclusions

In this study, ductile strain-hardening geopolymer composite materials were successfully designed based micromechanics framework and processed in laboratory conditions. The durability characteristic of FGC was characterized under different exposure conditions such as elevated temperatures, drying shrinkage, alkali-silica reaction, water permeation and accelerated corrosion. The following conclusions can be drawn from this study:

I. Ductile strain-hardening geopolymer was designed based on micromechanics theory to feature a tensile strain capacity more than 4% (400 times larger than regular geopolymer), thus exhibiting a “non-brittle” behavior in contrast with regular geopolymer materials.

II. Ductile strain-hardening geopolymer exhibited high temperature resistance, due to (1) tensile ductility that accommodates thermal expansion of solid phases (2) creation of a large connected pore network after fiber melting to release pore pressure.

III. Drying shrinkage of ductile strain-hardening geopolymer was found to be relatively higher than mortar. However, it is not a concern for restrained shrinkage cracking because its tensile strain capacity is one order higher than its shrinkage

strain. Instead of localized fracture, the ductile geopolymer will exhibit multiple microcracking behavior to strain and accommodate the shrinkage deformation.

IV. Alkali-silica reaction is not a concern for ductile strain-hardening geopolymer because the selected aggregates do not actively react with alkali.

V. Ductile strain-hardening geopolymer has lower corrosion rate than mortar. Furthermore, its ductile behavior prevents concrete cover spalling due to corrosion.

8.2 Future Work

While the work has successfully design new FGC with a tensile strain-hardening behavior and elucidated its behavior under various exposure conditions, more thorough characterization is needed in future to understand the fundamental mechanisms for the observed material behavior in this study. For example, what is the chemistry occurring in the geopolymer materials and how the chemistry influences the mechanics or mechanical properties of the materials. With this being understood, advanced modeling techniques needs to be developed to model these mechanisms with varying chemical and physical parameters; the models will be validated through well-controlled experimental studies and the modeling results can guild us to design future geopolymer composite material with optimal properties and target functionalities. For example, geopolymers with increased damage tolerance, reduced drying shrinkage, and ultra-high temperature resistance can be designed in future. In addition, it is important to understand the material behavior under combined environmental and mechanical loading conditions, which will establish the groundwork for its application in complex field conditions.

BIBLIOGRAPHY

[1] Daeik Kim, Hsuan-Ting Lai, George V. Chilingar, Teh Fu Yen., "Geopolymer formation and its unique properties," Environmental Geology, Vol. 51, NO. 1, October 2006, pp. 103-111

[2] Davidovits J., Proc. 2nd Intern. Conf. "Geopolymer 99," St. Quentin, 1999

[3] Davidovits J,: Proc. World Congress "Geopolymer 2005," St. Quentin, 2005

[4] Davidonits J. Geopolymer chemistry &applications 3rd edition, July 2011

[5] Motohiro Ohno, Victor C. Li., "A feasibility study of strain hardening fiber reinforced fly ash-based geopolymer composites," Construction and Building Materials, V. 57, April 2014, pp. 163-168

[6] Xiao Yao, Zuhua Zhang, Huajun Zhu, Yue Chen.," Geopolymerization process of alkali–metakaolinite characterized by isothermal calorimetry," Thermochimica Acta, V. 493, No. 1-2, September 2009, pp. 49-54

[7] Rattanasak, U., and Chindaprasirt, P., "Influence of NaOH Solution on the Synthesis of FA Geopolymer," Minerals Engineering, V. 22, No. 12, Oct. 2009, pp. 1073-1078

[8] Hardjito, D. Wallah, S. E. Sumajouw, D. M. J. and Rangan, B. V., "On the Development of FA-Based Geopolymer Concrete," ACI Materials Journal, V. 101, No. 6, Nov.-Dec. 2004, pp. 467-472

[9] Pacheco-Torgal, F. Castro-Gomes, J. and Jalali, S., "Alkali-Activated Binders: A Review. Part 2. About Materials and Binders Manufacture," Journal of Construction and Building Material, V. 22, No. 7, July 2008, pp. 1315-1322

[10] A. M. Mustafa Al Bakri, H. Kamarudin, M. Bnhussain, A. R. Rafiza, and Y. Zarina., "Effect of Na2SiO3/NaOH Ratios and NaOH Molarities on Compressive Strength of Fly-Ash-Based Geopolymer," ACI materials journal, V. 109, No. 48, September-October 2012, pp. 503-508

[11] Lucie Zuda, Robert C. Ernyal, "Measurement of linear thermal expansion coefficient of alkali-activated aluminosilicate composites up to 1000 ºC," Cement & Concrete Composites, V. 31, 2009, pp. 263-267

[12] John L. Provis, Chu Zheng Yong, Peter Duxson, Jannie S.J. van Deventer, "Correlating mechanical and thermal properties of sodium silicate-fly ash geopolymers," Colloids and Surfaces A: Physicochemical and Engineering Aspects, V. 336, 2009, pp. 57–63

[13] Daniel L.Y. Kong, Jay G. Sanjayan, “Damage behavior of geopolymer composites exposed to elevated temperatures,” Cement & Concrete Composites, V. 30, 2008, pp. 986-991

[14] Maurice Guerrieri, Jay Sanjayan, Frank Collins, “Residual compressive behavior of alkali-activated concrete exposed to elevated temperatures,” Fire Mater, V. 33, 2009, pp.51-62

[15] Valeria F.F. Barbosa, Kenneth J.D. MacKenzie, “Synthesis and thermal behaviour of potassium sialate geopolymers,” Materials Letters, V. 57, 2003, pp. 1477– 1482

[16] Prakash S. Bhat, Vivian Chang, Mo Li, “Effect of elevated temperature on strain-hardening engineered cementitious composites,” Construction and Building Materials, V. 69, 2014, pp. 370–380

[17] E. E. Holt, “Early Age Autogenous Shrinkage of Concrete,” Technical Research Institute of Finald, 2001

[18] G. W. Scherer, “Aging and Drying of Gels,” Journal of Non-Crystalline Solids, vol. 100, 1988, pp. 77-92

[19] Wallah SE, Rangan BV., “Low calcium fly ash based geopolymer concrete: long term properties,” Faculty of Engineering, Curtain University of Technology, Perth, Australia, 2006

[20] Sagoe-Crentsil K, Taylor A, Brown T., “Drying shrinkage and creep performance of geopolymer concrete,” Journal of Sustainable Cement-Based Materials, V. 2, No. 1, 2013, pp. 35-42

[21] A. Castel , S. J. Foster, T. Ng, J. G. Sanjayan, R. I. Gilbert., “Creep and drying shrinkage of a blended slag and low calcium fly ash geopolymer Concrete,” Materials and Structures, DOI 10.1617/s11527-015-0599-1, 2015

[22] Atis, C. D., Bilim, C., Celik, O., Karahan, O., “Influence of activator on the strength and drying shrinkage of alkali activated slag mortar,” Construction and Building Materials, V. 23, No. 1, 2007, pp. 548-555

[23] Ranjani Mosale Vijayakumar, “Evaluating shrinkage of fly ash-slag geopolymer,” Master thesis, University of Illinois at Urbana-Champaign, 2013

[24] N.K. Lee, J.G. Jang, H.K. Lee., “Shrinkage characteristics of alkali-activated fly ash/slag paste and mortar at early ages,” Cement & Concrete Composites, V. 53, 2014, pp. 239-248.

[25] S. Diamond, “Alkali Aggregate Reactions in Concrete: An Annotated Bibliography,” 1939-1991. Strategic Highway Research Program Report (SHRP-C/UWP-92-601), 1992, pp. 465

[26] B. Godard, M. de Rooij, J.G.M. Wood, “Guide to Diagnosis and Appraisal of AAR Damage to Concrete in Structures—Part 1—Diagnosis,” RILEM AAR-6.1

[27] Kevin J. Folliard, Michael D. A. Thomas, and Kimberly E. Kurtis, “Guidelines for the Use of Lithium to Mitigate or Prevent ASR,” The Transtec Group, Inc., No. 86, July 2003, FHWARD03047

[28] C. Larive, A. Laplaud, O. Coussy, “The role of water in alkali–silica reaction,” In Proceedings of the 11th International Conference on Alkali–Aggregate Reaction in Concrete, 2000, pp. 61–69

[29] ACI Committee 221, State of the Art Report on Alkali Aggregate Reactivity, ACI 221.1R-98, 1998, pp. 31

[30] G. Blight, M. Alexandre, “Alkali-Aggregate Reaction and Structural Damage to Concrete,” 2011, pp. 229

[31] Maarten A.T.M. Broekmans, “Deleterious Reactions of Aggregate with Alkalis in Concrete,” Mineralogy & Geochemistry, V. 74, 2012 pp. 279-364

[32] Kunal Kupwade-Patil, Erez N. Allouche, “Impact of Alkali Silica Reaction on Fly Ash-Based Geopolymer Concrete,” Journal of Materials in Civil Engineering, V. 25, No.1, January 2013, pp.131-139

[33] Kunal Kupwade-Patil, Erez Allouche, “Effect of alkali silica reaction (ASR) in geopolymer,” World of Coal Ash (WOCA) conference, May 9-12 2011, in Denver, CO, USA

[34] Raphaelle Pouhet, Martin Cyr, “Alkali–silica reaction in metakaolin-based geopolymer mortar,” Materials and Structures, V. 48, 2015, pp. 571-583

[35] Sindhunata, John L. Provis, Grant C. Lukey, Hua Xu, and Jannie S. J. van Deventer, “Structural Evolution of Fly Ash Based Geopolymers in Alkaline Environments,” Industrial & Engineering Chemistry Research, V. 47, 2008, pp. 2991-2999

[36] Hughes D., “Pore structure and permeability of hardened cement paste,” Magazine of Concrete Research, V. 37, No. 133, 1985, pp. 227-33

[37] Banthia N, Mindess S., “Water permeability of cement paste,” Cement and Concrete Research, V.19, No. 5, 1989, pp. 727-736

[38] Halamickova P, Detwiler RJ, Bentz DP, Garboczi EJ., “Water permeability and chloride ion diffusion in Portland cement mortars: relationship to sand content and critical pore diameter,” Cement and Concrete Research, V. 25, No. 4, 1995, pp. 790-802.

[39] Y. Ma, J. Hua, G. Ye, “The pore structure and permeability of alkali activated fly ash,” Fuel, V. 104, 2013, pp.771-780

[40] Morris, J., Hodges, S. “Corrosion of metals in fly ash-based geopolymers,” World Congress Geopolymer 2005: Geopolymer, Green Chemistry and Sustainable Development Solutions, 2005

[41] J.M. Miranda, A. Fernandez-Jimenez, J.A. Gonzalez, A. Palomo, “Corrosion resistance in activated fly ash mortars,” Cement and Concrete Research, V. 35, 2005, pp. 1210-1217

[42] D.M. Bastidas, A. FernaALndez-JimeALnez, A. Palomo, J.A. GonzaALlez, “A study on the passive state stability of steel embedded in activated fly ash mortars,” Corrosion Science, V. 50, 2008, pp. 1058-1065

[43] P. Chindaprasirt , W. Chalee, “Effect of sodium hydroxide concentration on chloride penetration and steel corrosion of fly ash-based geopolymer concrete under marine site,” Construction and Building Materials, V. 63, 2014, pp.303-310

[44] Yodmunee, S., Yodsujai, W., “Study on corrosion of steel bar in fly ash based geopolymer concrete,” Proceedings of International Conference on Pozzolan, Concrete and Geopolymer, 24–25 May 2006, Khon Kaen

[45] M. Olivia, H.R. Nikraz, “Corrosion performance of embedded steel in fly ash geopolymer concrete by impressed voltage method,” Incorporating Sustainable Practice in Mechanics and Structures of Materials, 2010, pp. 781-786

[46] Abdul-Hamid J. AI-Tayyib, Mesfer M. AI-Zahran, “Corrosion of Steel Reinforcement in Polypropylene Fiber Reinforced Concrete Structures,” ACI Materials journal, V. 87, No. 12, 1990, pp. 108-113

[47] Mustafa Sahmaran, Victor C. Li, Carmen Andrade, “Corrosion Resistance Performance of Steel-Reinforced Engineered Cementitious Composite Beams,” ACI Materials journal, V. 105, No. 28, 2008, pp. 243-250

[48] ASTM C39/C39M − 15a, Standard Test Method for Compressive Strength of Cylindrical Concrete Specimens

[49] ASTM C157/C157M − 08 (Reapproved 2014), Standard Test Method for Length Change of Hardened Hydraulic-Cement Mortar and Concrete

[50] ASTM C1260 – 14, Standard Test Method for Potential Alkali Reactivity of Aggregates (Mortar-Bar Method)

[51] Ferraro, C.C., Report of Investigation of 78 stone for the use as coarse aggregate in prestressed concrete. 2005

[52] S.H. Okba, A.S. El-Dieb, M.M. Reda, “Evaluation of the corrosion resistance of latex modified concrete (LMC),” Cement and Concrete Research, V. 27, No. 6, 1997, pp. 861-868

[53] F. Collins, S. J.G., “Effect of Pore Size Distribution on Drying Shrinkage of Alkali-Activated Slag Concrete,” Cement and Concrete Research, V. 30, 2000, pp. 1401-1406

[54] Kevin M. Smith, Andrea J. Schokker, Paul J. Tikalsky, “Performance of Supplementary Cementitious Materials in Concrete Resistivity and Corrosion Monitoring Evaluations,” ACI Materials journal, V. 101, No. 43, 2004, pp. 385-390

[55] Mustafa Sahmaran, Mo Li, Victor C. Li, “Transport Properties of Engineered Cementitious Composites under Chloride Exposure,” ACI Materials journal, V. 104, No. 66, 2007, pp. 604-611

[56] ASTM G1 − 03 (Reapproved 2011), Standard Practice for Preparing, Cleaning, and Evaluating Corrosion Test Specimens

[57] Isaac A. Wootton, Lisa K. Spainhour, Nur Yazdani, “Onset and rate of corrosion in CFRP wrapped reinforced concrete cylinders,” "The Third International Conference on Composites in Infrastructure," 2002, San Francisco, CA

[58] Tamer A. El Maaddawy, Khaled A. Soudki, “Effectiveness of Impressed Current Technique to Simulate Corrosion of Steel Reinforcement in Concrete,” Journal of Materials in Civil Engineering, V. 15, 2003, pp. 41-47

[59] ASTM C1231/C1231M – 14, Standard Practice for Use of Unbonded Caps in Determination of Compressive Strength of Hardened Concrete Cylinders

[60] Victor C Li and Hwai-Chung Wu, “Conditions for pseudo strain-hardening in fiber reinforced brittle matrix composites,” Applied Mechanics Reviews, V. 45, No.8, 1992, pp.390-398.

[61] Victor C. Li, “From Micromechanics to Structural Engineering – The Design of Cementitious Composites for Civil Engineering Applications,” JSCE Journal of Structural Mechanics and Earthquake Engineering, V. 10, No.2, 1993, pp. 37-48

[62] Mo Li, “Multi-Scale Design for Durable Repair of Concrete Structures,” Doctor of Philosophy, University of Michigan, Ann Arbon, MI, USA, 2009,

[63] Raut, Nikhil, “Response of High Strength Concrete Columns under Fire-Induced Biaxial Bending.,” PhD, Michigan State University, MI, USA, 2011

[64] Henrik Stang, Victor C. Li, Herbert Krenchel, “Mechanics of Fiber Reinforced Concrete: Materials Design for Structural Applications,” Research Studies Press Limited, 2003